Article

Stacking Faults Assist Lithium-Ion Conduction in a Halide-Based Superionic Conductor

Elias Sebti, Hayden A. Evans, Hengning Chen, Peter M. Richardson, Kelly M. White, Raynald Giovine, Krishna Prasad Koirala, Yaobin Xu, Eliovardo Gonzalez-Correa, Chongmin Wang, Craig M. Brown, Anthony K. Cheetham, Pieremanuele Canepa,* and Raphaële J. Clément*

Cite This: *J. Am. Chem. Soc.* 2022, 144, 5795−5811

Read Online

ACCESS | Metrics & More | Article Recommendations | Supporting Information

ABSTRACT: In the pursuit of urgently needed, energy dense solid-state batteries for electric vehicle and portable electronics applications, halide solid electrolytes offer a promising path forward with exceptional compatibility against high-voltage oxide electrodes, tunable ionic conductivities, and facile processing. For this family of compounds, synthesis protocols strongly affect cation site disorder and modulate Li$^+$ mobility. In this work, we reveal the presence of a high concentration of stacking faults in the superionic conductor Li$_3$YCl$_6$ and demonstrate a method of controlling its Li$^+$ conductivity by tuning the defect concentration with synthesis and heat treatments at select temperatures. Leveraging complementary insights from variable temperature synchrotron X-ray diffraction, neutron diffraction, cryogenic transmission electron microscopy, solid-state nuclear magnetic resonance, density functional theory, and electrochemical impedance spectroscopy, we identify the nature of planar defects and the role of nonstoichiometry in lowering Li$^+$ migration barriers and increasing Li site connectivity in mechanochemically synthesized Li$_3$YCl$_6$. We harness paramagnetic relaxation enhancement to enable ^{89}Y solid-state NMR and directly contrast the Y cation site disorder resulting from different preparation methods, demonstrating a potent tool for other researchers studying Y-containing compositions. With heat treatments at temperatures as low as 333 K (60 °C), we decrease the concentration of planar defects, demonstrating a simple method for tuning the Li$^+$ conductivity. Findings from this work are expected to be generalizable to other halide solid electrolyte candidates and provide an improved understanding of defect-enabled Li$^+$ conduction in this class of Li-ion conductors.

Ball mill synthesis → Stacking fault generation → Improved Li$^+$ conduction. Layer shift. Li$^+$.
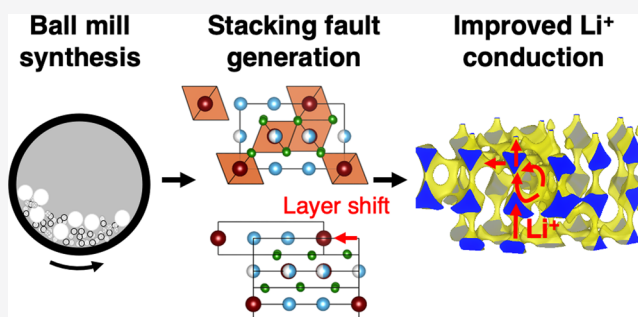
1. INTRODUCTION

Achieving greater market penetration for electric vehicles today hinges on gaining the public's trust in their durability, versatility, and safety. In recent years, Li-ion solid-state batteries (SSBs) with inorganic solid electrolytes (SEs) have gained traction as safer and potentially higher energy density alternatives to the commercial liquid electrolyte (LE) cells. Replacing the combustible organic LE with a nonflammable SE severely lessens the consequences of an internal short-circuit and may also extend the range of operating temperatures for the cell.[1,2] Beyond safety, the lack of any liquid component opens the door to bipolar stack SSB architectures that enhance battery module energy density and lower manufacturing costs as cells no longer have to be individually packed to avoid leakage.[3,4] Notably, Li-ion SEs have transference numbers close to 1 which could allow for faster charging than LE cells when paired with high ionic conductivities.[1,5−9]

Since a 2018 publication from Asano et al.[10] reported high Li$^+$ conductivities in Li$_3$YCl$_6$ (LYC) and Li$_3$YBr$_6$ (LYB), lithium-containing halide ternaries have emerged as appealing SE candidates owing to their promising room temperature conductivities, strong oxidative stability to high potentials, and hence compatibility with oxide-based cathode materials.[10,11] Sulfide SEs rely on a body-centered cubic (BCC) anion sublattice to ensure low migration barriers and fast Li$^+$ conduction.[12−14] Oxides require aliovalent doping to achieve appreciable Li$^+$ conduction through concerted migration, enabled by greater Li$^+$ concentrations and concomitant occupation of high energy Li sites.[15−17] In contrast, halide SEs exhibit high Li$^+$ conductivities at stoichiometric Li contents despite having a close packed anion lattice because of a combination of intrinsic vacancies and reduced Coulombic interactions between the migrating Li$^+$ and monovalent anions.[18−20] Recent studies have also led to further improvements in conduction through both isovalent[21,22] and aliovalent

substitution,[23−28] as well as anion mixing.[29] Ternary lithium halides, especially chloride- and fluoride-based chemistries, also resist oxidation against high-voltage oxide electrodes on charge due to the strong electronegativity of their anionic species. This could enable the use of high-voltage cathode compositions, such as $LiNi_{0.5}Mn_{1.5}O_4$.[11,18,30]

Asano et al.[10] were the first to observe that the ionic conductivity of LYC decreases from ≈0.51 mS cm^{-1} after annealing a mechanochemically synthesized sample. This behavior, especially when compared to the opposite evolution for the LYB analog, is surprising as one would expect the increased crystallinity induced by annealing to favor long-range conduction. Later, *ab initio* molecular dynamics (AIMD) calculations reported by Wang et al.[18] predicted that the LYC structure proposed by Asano et al.[10] should yield conductivities between ≈4.5 and ≈14 mS cm^{-1}, with an activation energy for Li$^+$ ion migration of 0.03 eV (all confidence intervals listed are 1σ), far smaller than the ≈0.40 eV experimentally measured value. Using X-ray pair distribution function (PDF) analysis, Schlem et al.[31] shed some light on the discrepancies between predicted and experimentally determined conduction properties when they tied synthesis-induced cation site disorder to the conductivity and activation energy of the sample for Li_3ErCl_6, a compound isostructural to LYC. Mechanochemical synthesis induces greater Er disorder, generating polyhedral distortions that open bottleneck transition areas and facilitate Li$^+$ migration. Notably, their PDF analysis of LYC was precluded by fluorescent behavior under X-ray illumination due to their choice of wavelength (λ = 0.5594 Å) that limited the accuracy of the interpretation of the data. The propensity for disorder on the yttrium sublattice of LYC was recently demonstrated by Ito et al., who showed using *in situ* X-ray diffraction that two polymorphs of LYC are obtained when heating a mixture of LiCl and YCl$_3$ powders.[32] A metastable, more ionically conductive β-LYC phase is at 450 K but gives way above 600 K to the more stable, commonly reported α-LYC polymorph, which retains the identical hexagonal close packed Cl anion sublattice but differs in its arrangement of Y^{3+} cations.

Functional inorganic materials with layered crystal structures are exceptionally prevalent and find use as Li-ion battery cathodes, superconductors, and catalysts. Stacking faults can be pervasive in these materials with synthesis-dependent concentrations, but they are rarely investigated in depth as they are notoriously difficult to model and understand, both experimentally and computationally. Unfortunately, this does not allow for an atomic understanding of the dependence of the properties of interest in the material's defective crystal structure. The presence of stacking faults can be of paramount importance to ionic conduction and redox properties as exemplified by Ni(OH)$_2$, a double hydroxide material commonly used as a cathode in Ni hydride metal batteries, where stacking faults greatly ameliorate the electrochemical performance.[33] Furthermore, $Na_4P_2S_6$ is a Na-ion solid electrolyte where stacking faults generated from a precipitation synthesis stabilize a conductive high temperature phase at room temperature.[34] A number of other relevant examples also exist in Li- and Na-ion transition metal oxide cathodes,[35−48] Ag nanoparticle catalysts,[49] and ionic conductors.[50,51]

The three-dimensional LYC crystal structure (space group $P\bar{3}m1$) investigated in this study bears a strong resemblance to the layered structure of YCl$_3$ (space group $C2/m$), where both structures exhibit a hexagonal close-packed Cl$^-$ anion

sublattice (ABAB) and a hexagonal Y^{3+} arrangement. However, YCl$_3$ contains (002) planes of octahedral cation voids, in contrast to LYC, which has Y^{3+} and Li$^+$ ions distributed throughout its (001) and (002) planes. Deng et al.[52] recently demonstrated that YCl$_3$ is amenable to polymorphism, especially with respect to the related BiI$_3$-type structure which shows an alternate ABCABC anion stacking arrangement. According to their calculations, the energy difference between the two structure-types is ≈0.1 kJ mol^{-1} (≈1 meV atom^{-1}), suggesting that alternate stackings, or even stacking faults, are possible in YCl$_3$-type structures. Stacking faults have in fact been mentioned for LYC, LYB, and a mixed anion Li$_3$YCl$_3$Br$_3$ halide composition,[10,29] although no detailed analysis of these planar defects or of their impact on ion conduction has been undertaken to date, preventing the establishment of robust design rules for this family of solid electrolytes.

In this study, we investigate the crystal structure of LYC and its conduction properties as a function of synthesis method, using a combination of synchrotron X-ray diffraction (XRD), neutron diffraction, cryogenic transmission electron microscopy (cryo-TEM), high-resolution ^{6,7}Li and ^{89}Y nuclear magnetic resonance (NMR), electrochemical impedance spectroscopy (EIS), and density functional theory (DFT) calculations, to reveal a complex metastable defect landscape. We establish a link between these complex structural defects and Li$^+$ ion conduction. Our in-depth analysis of X-ray patterns demonstrates the presence of a high concentration of previously unreported stacking faults in mechanochemically synthesized LYC that generate face-sharing YCl$_6^{3-}$ octahedra. EIS, pulsed field gradient-NMR (PFG-NMR), and computational investigation of defect structural models reveal that the stacking faults facilitate Li$^+$ conduction through the structure by lowering Li$^+$ migration barriers and generating more interlayer channels for Li$^+$ transport. However, the defects are shown to be metastable with some disappearing after heat treatment at temperatures as low as 333 K (60 °C). As the defect concentration decreases, Li$^+$ transport is hindered and the ionic conductivity of the sample decreases. These findings emphasize the importance of defects in promoting long-range Li$^+$ conduction in halide-type SEs[53] and suggest that the conduction properties in these structures are enhanced by high defect concentrations associated with metastable states.

2. RESULTS

2.1. Current Understanding of the Li$_3$YCl$_6$ Crystal Structure.
The first report of LYC by Steiner et al.[54] proposed LYC crystallizes in an orthorhombic crystal structure. More recently, the trigonal ($P\bar{3}m1$) description of LYC was put forth by Asano et al.[10] and is now deemed to be more appropriate. In the $P\bar{3}m1$ structure, both Li$^+$ and Y^{3+} ions are octahedrally coordinated by Cl$^-$ ions arranged onto a hexagonal close-packed lattice. However, Rietveld refinements of diffraction patterns of mechanochemically synthesized LYC by Asano et al.[10] indicate that Y^{3+} disorder exists over four Wyckoff sites: 1a (0,0,0), 2d (1/3, 2/3, 0.5), and (1/3, 2/3, 0), and a 1b site (0, 0, 0.5) (Figure 1b). This disorder was previously suggested to be the result of the low energy of formation of Y^{3+} and Li$^+$ antisite defects.[18]

An X-ray diffraction study by Schlem et al.[31] investigated synthesis-dependent disorder in LYC and a crystallographic isomorph, Li$_3$ErCl$_6$. For Li$_3$ErCl$_6$, the authors reported that Er atoms fully occupy the $P\bar{3}m1$ 1a site denoted as M1 and
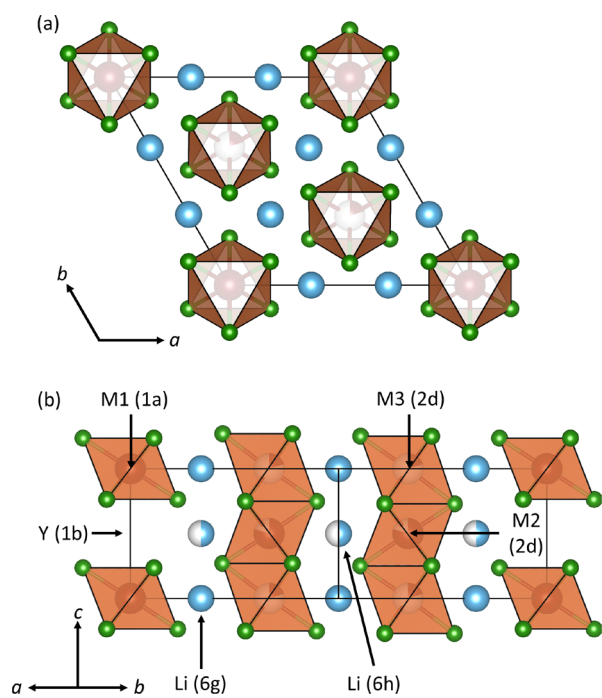
Figure 1. Reported $P\bar{3}m1$ structure of LYC shown from different angles: (a) structure viewed down the c-axis; (b) annotated side view of the LYC crystal structure. The structure exhibits full Y occupancy at the M1 (0, 0, 0) position, and split Y occupancy over the M2 (1/3, 2/3, 0.5) and M3 (1/3, 2/3, 0) positions. The Wyckoff positions are denoted in parentheses.[55] Li positions, as well as the 1b Y site reported by Asano et al.,[10] are also included.

partially occupy the (1/3, 2/3, 0.5) and (1/3, 2/3, 0) 2d sites denoted as M2 and M3, respectively. With only the M1 and M2 sites fully occupied, the structure is referred to as M1−M2. If the structure has only the M1 and M3 sites fully occupied, it is referred to as M1−M3. Though X-ray characterization of LYC was hindered by fluorescence for Schlem et al. in their study, the insight gained on Li_3ErCl_6 proved relevant as the bonding behavior and ionic radii of Er^{3+} and Y^{3+} (0.890 and 0.900 Å, respectively) are quite similar. They reported that mechanochemical synthesis of Li_3ErCl_6 produces a high ionic conductivity sample with an almost entirely M1−M3 atomic arrangement, while a high temperature annealing synthesis yielded a reduced ionic conductivity sample with an almost entirely M1−M2 atomic arrangement. A follow-up investigation of LYC by Schlem et al.[55] using neutron diffraction indicated no appreciable Li^+ occupancy preference between the $P\bar{3}m1$ 6g and 6h sites (Figure 1b), which in turn indicated that the disordered Y^{3+} occupancy did not appear to affect the Li^+ substructure. However, we will note that the samples studied by Schlem et al.[55] were both annealed: one for a week at 823 K (550 °C) and the other first ball milled and then annealed for 5 min at 823 K (550 °C).

Another recent study by Ito et al. investigated the synthesis of LYC from its binary precursors, LiCl and YCl_3, with *in situ* X-ray diffraction.[32] Diffraction patterns taken throughout a temperature ramp demonstrated that a new, metastable β-LYC polymorph ($P\bar{3}c1$) appears above 450 K and is eventually consumed in favor of the previously reported α-LYC polymorph ($P\bar{3}m1$) above 600 K. EIS measurements showed that the β-phase has a higher Li^+ conductivity (0.12 mS cm⁻¹) than the α-phase (0.014 mS cm⁻¹), which the authors

attributed to broadening of the Li^+ conduction pathways caused by the higher energy Y^{3+} cation arrangement in the β-phase. This study showed that the phase transition between the β and α polymorphs relies on migration of Y^{3+} along the c-axis, which is kinetically hindered at low temperatures and explains the metastability of the β-phase. Importantly, the authors conclude that the β-LYC phase is not formed when the precursors are ball milled together as all of the X-ray diffraction peaks reported by Schlem et al. could be indexed to α-phase reflections.

2.2. Diffraction Characterization of Li₃YCl₆. Ball milled (BM-LYC) and solid-state (SS-LYC) samples of Li_3YCl_6 (LYC) were prepared and examined using neutron and X-ray diffraction. The LYC synthesis procedures have been reported elsewhere,[31,55] with the distinction that our BM-LYC samples were not annealed after mechanochemical milling and instead studied at specific temperatures *in situ*. When it comes to structural analysis, the proposed $P\bar{3}m1$ structure is relatively accurate for describing the average structure of LYC. However, as shown in previous work,[10,31] there is still some ambiguity as to the Y^{3+} ordering particularly in BM-LYC. Furthermore, previous models were developed without using X-ray synchrotron diffraction data, which is more sensitive to Y^{3+} positions relative to neutron diffraction data. As such, our work utilizing high quality X-ray synchrotron diffraction data reveals important insights into the LYC structure. The importance of synchrotron X-ray data is demonstrated in Figure 2, with the
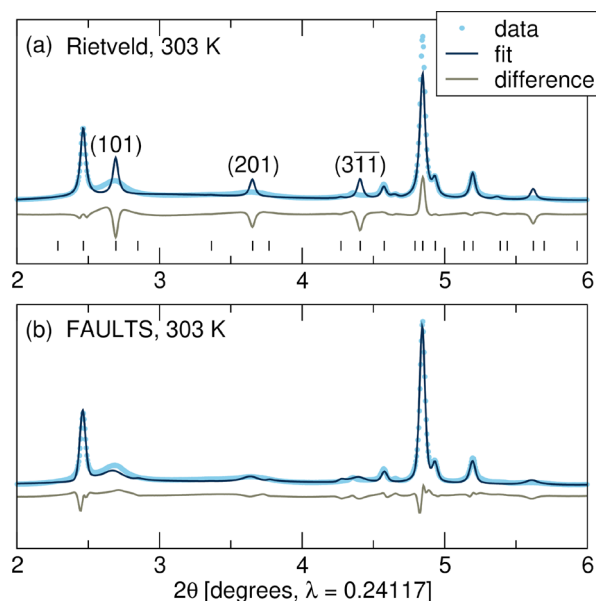

Figure 2. Comparison between (a) Rietveld analysis and (b) FAULTS analysis of X-ray diffraction data [17-BM, wavelength = 0.241 17 Å] of ball milled Li_3YCl_6 at 303 K. The Rietveld model used a fully occupied M1 site and a fixed value of 70/30 Y occupancy split over the M2 and M3 sites, respectively, as was reported previously.[55]

presence of significant broadening and even disappearance of reflections associated with specific hkl planes. This broadening and loss of intensity have previously been attributed to decreased crystallinity of the materials due to ball milling.[31] However, when certain hkl reflections in a diffraction pattern are systematically impacted, such as broadened or even eliminated, this is usually indicative of stacking faults within a sample.[43,44] Antisite disorder can also be ruled out as these
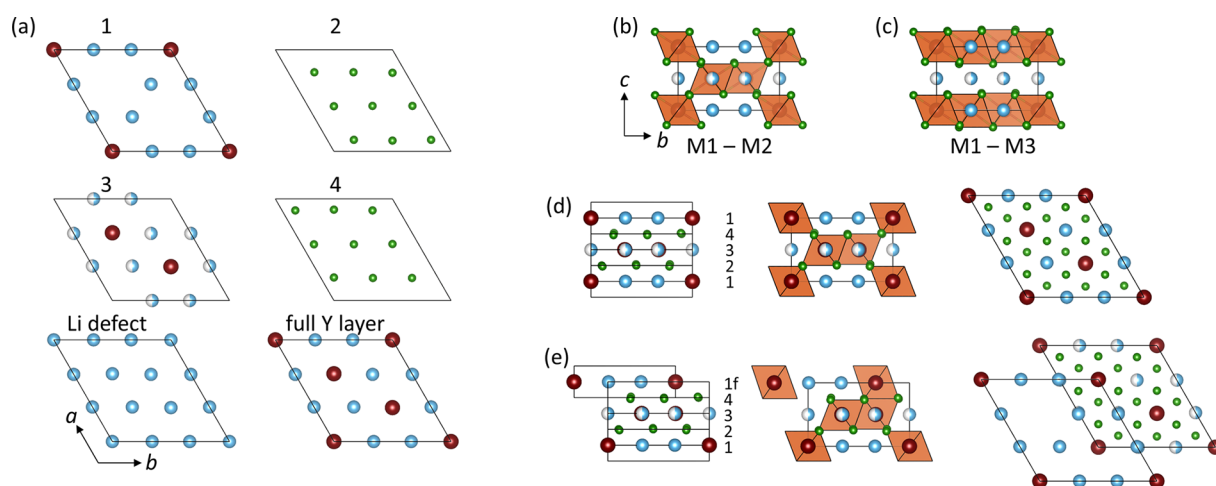
Figure 3. Construction of stacking fault models: (a) individual layers. Atom legend: red for Y; blue for Li; green for Cl. Side on view of the (b) M1−M2 and (c) M1−M3 models proposed by Schlem et al.[55] (d) M1−M2 layered model that serves as the starting point for the stacking fault model construction (e) illustration of the (1/3, 2/3) layer 1 fault that is responsible for the majority change in the X-ray diffraction pattern. One notes that the Li⁺ substructure is essentially unchanged by this fault and the major consequence is the creation of face sharing Y−Cl species along the center of the unit cell.

defects would not induce selective broadening. Stacking faults are notorious for complicating the intensities and peak shapes of Bragg reflections in powder diffraction patterns,[56] making Rietveld analysis unreliable. Using the $P\bar{3}m1$ structural model proposed by Schlem et al.[55] as a reference, the most impacted hkl reflections in the BM-LYC patterns are the (101), (201), and (3$\bar{1}\bar{1}$). These reflections, as we discuss below, are predominantly caused by planes of Y atoms. As shown in Figure 2a, the peaks in the experimental data are much broader (or absent) relative to the peak intensity expected from the Rietveld model. Figure 2b shows a fit using a stacking fault model, which we believe to be more appropriate for describing BM-LYC. Though there are likely many other structural intricacies present in disordered compounds like LYC (regardless of preparation), our results suggest that LYC prepared via ball milling is particularly susceptible to stacking faults. Cryo-TEM on the BM-LYC was attempted to obtain direct evidence for the presence of stacking faults, but the sample's susceptibility to beam damage precluded any observation of the sample in its pristine state (see Figure S1a,b).

Overall, we find synchrotron X-ray diffraction data to be more useful than neutron diffraction data for the analysis of the structure of LYC samples. Though neutron diffraction was expected to provide additional insight, analysis of the neutron data, as illustrated in Figure S2, is complicated by the large chloride neutron scattering signal relative to the other elements (combined scattering lengths of Cl ≈ 9.577 fm × 6 = 57.462 fm, Li ≈ −1.90 fm × 3 = −5.7 fm, and Y ≈ 7.75 fm). Figure S2 illustrates how, even when using drastically different stacking fault models to describe the 303 K BM-LYC diffraction data, the difference between the fits is minimal. This tolerance to changing stacking fault models when fitting the neutron data is a result of the stacking faults involving predominantly Y atoms, as detailed below, which are better observed with X-rays as opposed to neutrons.

To construct Y atom centric stacking fault models, we used the proposed $P\bar{3}m1$ LYC structure as a starting point.[55] This structure captures allowed hkls relatively well (Figure 2a) and indicates that the hkl reflections associated with Y atoms are

the most affected by stacking faults. We constructed a layer-by-layer model of the 3D structure that was initially "ordered", but into which Y³⁺ disorder could be introduced with relative ease. Our starting stacking sequence reproduced the proposed M1−M2 structure for Li_3YCl_6 from Schlem et al.[31] As can be seen in Figure 3a, the layers used to construct the stacking fault model include two Cl layers, a Li defect layer, as well as three Y/Li layers that have Y atoms located at either the (0,0), (1/3, 2/3), and (2/3, 1/3) or all of those sites. Figure S3 illustrates in the form of a flowchart how the fault model refines the percent occurrence of each layer as the layer sequence deviates from the one present in the M1−M2 structure, all the while retaining trigonal symmetry. Figure 3b illustrates the M1−M2 model from Schlem et al.,[31] and Figure 3d illustrates the layer sequence used to build the starting M1−M2 structure.

As can be seen in Figure 3a, layer 1 has Y atoms only at the (0, 0) position. The fault that causes the broadening/loss of the (101), (201), and (3 $\bar{1}\bar{1}$) peaks is comprised of the two equally likely (1/3, 2/3) and (2/3, 1/3) faults of layer 1 (as illustrated in Figure 3e). This fault explains why the proposed average model by Schlem et al.[31,55] is relatively accurate in describing the LYC structure, as it introduces face sharing columns of Y−Cl octahedra at the (1/3, 2/3) and (2/3, 1/3) positions that propagate along the c-axis. In the $P\bar{3}m1$ structure, this fault is approximated by allowing Y³⁺ to occupy M3 sites (Figure 1). However, the $P\bar{3}m1$ model is inappropriate as it splits Y³⁺ occupancy over the M2 and M3 sites, with a combined crystallographic site occupancy of 1 (to charge balance the model). The issue is that if the layer 1 fault exists and one attempts to explain the structure using the $P\bar{3}m1$ model, then the occupancy of M3 should be shared with the M1 sites, not the M2 sites. Furthermore, though the fault model rationalizes why M3 occupancy exists in the $P\bar{3}m1$ model, it is unclear why there would be M2 sites without full occupancy. This discrepancy can be resolved by introducing Li defect layers with Li⁺ ions on all possible sites that remove Y³⁺ occupancy from the M2 sites.

Figure 4 shows comparative fits of the BM-LYC diffraction data at 303 K with various stacking fault models. Two models of faults and defect layers were found to best fit the diffraction
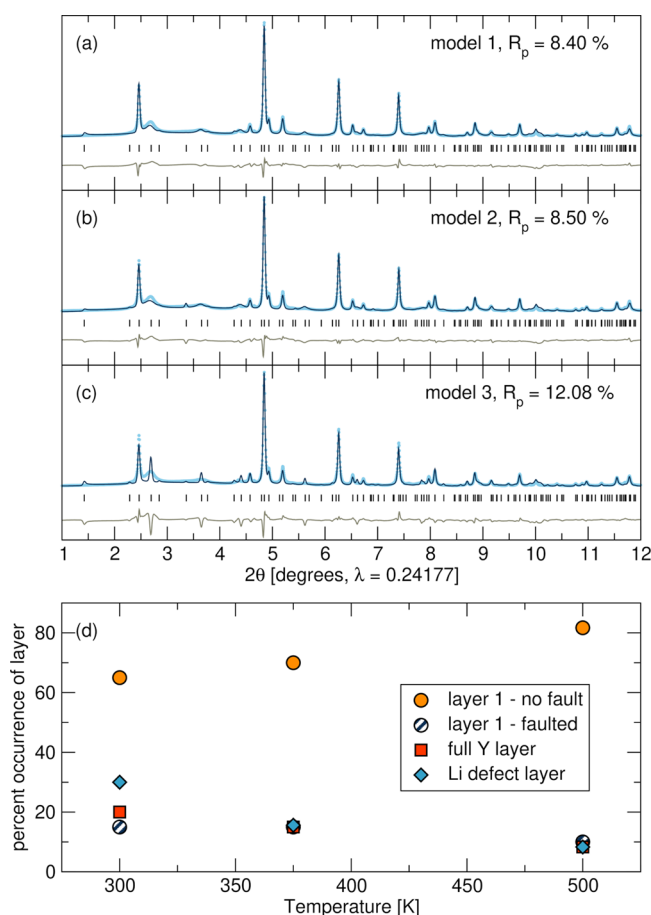
Figure 4. Results from FAULTS refinements of synchrotron X-ray diffraction data [17-BM, APS] of the BM-LYC sample at 303 K with and without certain faults/defect layers included. (a) Model 1 fit. This model exhibits layer 1 Y-fault [(1/3, 2/3) and (2/3, 1/3) shift], Li defect layer, and full Y layer occurrences of 15%, 30%, and 20%, respectively. The layer unit cell dimensions were refined to a = 11.206 75(4), c = 3.029 71(9) Å where a layer unit cell is a three layer slab comprising a Li/Y layer bound by two Cl layers. (b) Model 2 fit. This model has a layer 1 Y-fault [(1/3, 2/3) and (2/3, 1/3) shift] occurrence of 22% and a Li defect layer occurrence of 17%. The layer unit cell was refined to a = 11.203 37(3), c = 3.023 51(7) Å. (c) Model 3 fit. This fit illustrates the effect of using only the full Y layer and Li defect layer. Note how, by not using any layer 1 fault [(1/3, 2/3) and (2/3, 1/3) shift], the peak broadening beneath 5°2θ is not appropriately captured. The full Y layer occurrence is at 25%, and the Li-defect layer is at 50%. The layer unit cell dimensions were refined to a = 11.206 40(5) and c = 3.018 45(2) Å, respectively. For clarity, the 2θ range plotted in (a), (b), and (c) extends from 1 to 12°, but the refinements were performed between 1 and 15°. The tick marks shown correspond to expected hkl reflections for the proposed average structure (space group $P\bar{3}m1$, as shown in Figure 2a). (d) Percent occurrence for layers in model 1 as temperature is increased, as determined from FAULTS refinement of X-ray diffraction data [17-BM, APS]. Error estimates are one standard deviation.

data of BM-LYC, denoted as model 1 and model 2 hereafter. Model 1 is the preferred of these two models as it better explains the temperature evolution of the diffraction data of the BM-LYC sample. While models 1 and 2 are almost identical, model 1 also includes the "full Y layer" as a possible occurrence. The full Y layer is used to emulate the Y/Li layers that exist in the M1−M3 structure (Figure 3c) reported by Schlem et al.[31] We note here that the inclusion of full Y

layers in model 1 requires an equivalent amount of Li defect layers so as to maintain 3−1−6 stoichiometry and to charge balance the full Y layer. Inclusion of Li defect layers significantly improves the fits (see Figure S4). The presence of Li defect layers also explains some of the structural changes observed via NMR upon heating the BM-LYC, as discussed in section 2.4.

Figure 4a shows the model 1 fit, which has a 15% occurrence of the layer 1 fault [(1/3, 2/3) and (2/3, 1/3) shift], as well as a 20% occurrence of the full Y layer. Interestingly, the fit is improved by including more Li defect layers than is necessary to charge-balance the full Y layers. Figure 4b shows the model 2 fit, which has more layer 1 faults (22% occurrence) and fewer Li defect layers (17%) relative to model 1. Figure 4c (model 3) illustrates how inappropriate it is to exclusively rely on the M1−M3 layer and Li defect layers to simulate the pattern, as doing so does not lead to the observed peak broadening.

The BM-LYC structure was characterized via diffraction at various temperatures between 303 and 500 K. The evolution of the percent occurrence of the different layers accounted for in model 1 (at 303, 375, and 500 K) is plotted in Figure 4d. As can be seen from the plot, all faults/defects decrease as temperature increases, with the overall structure becoming more like the M1−M2 model. The Li defect layer used for modeling accounts for two types of Li layers: the Li layer required to charge-balance the existence of the full-Y layer, as well as any Li rich defects. Though these two types of Li layers might differ in Li content/arrangement, the use of one type of Li layer is an effective approximation for both layers because Li has minimal X-ray scattering contribution relative to Y and Cl atoms. The main purpose of including a Li defect layer is to account for a lack of Y scattering density in the X-ray diffraction data. At 303 K, the percent occurrence of the Li defect layer is greater than the necessary amount to charge-balance the full Y layer. This indicates that the BM-LYC compound is off-stoichiometric and best thought of as $Li_{3+3x}Y_{1-x}Cl_6$. At 375 and 500 K, the Li defect layer occurrence approximately matches the full Y layer, indicating that the compound is closer to the expected Li_3YCl_6 stoichiometry. In contrast, a refinement using model 2 indicates that Li defect layers still exist at 500 K. One may understand now why model 2 is less preferred, as these types of defects are likely to disappear completely at elevated temperature.

A BM-LYC composition of $Li_{3+3x}Y_{1-x}Cl_6$ at 303 K is difficult to ascertain from refinements alone. However, further evidence for off-stoichiometry in the room temperature sample comes from the emergence of an LiCl phase upon exposure to elevated temperatures, as discussed in section 2.4. If LiCl were to appear from the decomposition of LYC, we would expect to also observe diffraction peaks corresponding to YCl_3, which we do not. Hence, LiCl is likely precipitating out of the LYC phase, which suggests the presence of Li-rich regions in the LYC structure.

We now turn our attention to the SS-LYC sample. While the SS-LYC is prepared using a traditional solid-state method and involved repeated regrinding and reheating steps, this sample contains multiple phases. This can be inferred from the diffraction patterns shown in Figures S5 and S6. Figure S5 illustrates how the SS-LYC pattern obtained upon ramping up to 500 K shares features that are identical in shape and intensity to those observed in the BM-LYC sample held at 500 K for 50 min (both patterns were collected under identical conditions). Such shared features between the two types of

LYC samples are only seen in the high temperature data sets. Unfortunately, simply subtracting the BM-500 K 50 min pattern from the SS-LYC 500 K pattern does not produce a pattern of sufficient quality for Rietveld refinement. As can be seen from Figure S6, the LiCl peak present in the SS-LYC 300 K pattern decreases in intensity after heating to 500 K, implying that LiCl (and other components of the multiphasic SS-LYC sample) is still reacting upon heating to 500 K. The presence of the β-LYC polymorph was ruled out based on a Rietveld refinement presented in Figure S7. Its absence agrees well with the results from Ito et al. as our week-long synthesis was conducted at 823 K, far outside of the reported temperature stability window for the β-phase.[32] Electron diffraction measurements obtained via cryo-TEM (Figure S1c,d) confirm the presence of domains containing stacking faults in SS-LYC. Streaks in an electron diffraction pattern have been widely reported as indications of stacking faults[57−59] and provide unquestionable evidence that the LYC layered structure is capable of experiencing these planar defects.

Overall, as the SS-LYC sample is multiphasic with one of those constituent phases containing stacking faults (the BM-LYC-like features), we are unable to develop reliable structural models to fit its diffraction patterns.

2.3. Computational Analysis of Li−Y Orderings and Stacking Faults.

With compelling evidence for the presence of stacking faults from the diffraction analysis, we turned to theoretical simulations to better understand the propensity for disorder on the Y/Li lattices in LYC. Specifically, computing the energies of different LYC structural models with DFT offers insight into the most probable Li−Y arrangements in the structure.

Starting from the LYC unit cell (with space group $P\bar{3}m1$) as reported by Asano et al.[10] which includes four possible Y positions (see section 2.1), 237 distinct Li/Y arrangements were enumerated.[60] Of these, 76 are models with 3 formula units ($Li_9Y_3Cl_{18}$), while 161 are supercells including up to 6 formula units ($Li_{18}Y_6Cl_{36}$). In parallel, another set of structures was enumerated starting from specific stacking fault models identified by X-ray diffraction (see section 2.2), comprising up to 15 formula units ($Li_{45}Y_{15}Cl_{90}$) of LYC. In these stacking fault models, Li appears with fractional occupation, which we address using the same enumeration procedure as mentioned above. In total, 285 unique orderings were computed, of which 48 are symmetrically distinct stacking fault models, using DFT within the SCAN meta-GGA approximation. This level of theory appears adequate for the simulation of LYC and its structural features (see section S3 of the Supporting Information).

The relative stability of each LYC ordering was assessed in terms of its decomposition into the LiCl and YCl_3 binary compounds that share the same composition line. Notably, all the LYC orderings (including the stacking fault models) considered here always decompose into LiCl and YCl_3, in agreement with previous investigations.[18] The relative instability of the different LYC models is quantified by the energy above the convex hull, i.e., the propensity of LYC to decompose into LiCl and YCl_3. Structural models with energies above the convex hull of ≤30 meV atom^{-1} are likely to be stabilized by entropy contributions at ≈298 K (or higher temperature) and hence may be accessible via high-temperature or high-energy mechanochemical synthesis protocols.

Figure 5 plots the distribution of energy above the hull of the bulk orderings and stacking fault orderings considered in
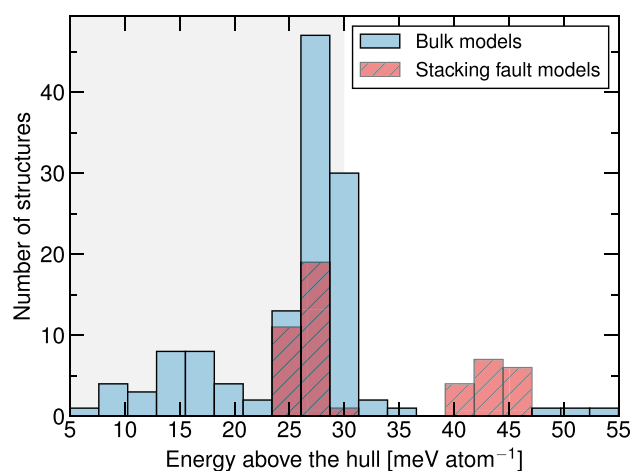

Figure 5. Distribution of predicted Li/Y orderings in Li_3YCl_6 vs their relative thermodynamic stability, expressed as energy above the hull. Some of the 237 bulk orderings are shown with blue bars, whereas the 48 stacking faults are shown by the red-hatched bars. Energetically accessible orderings below the 30 meV atom^{-1} threshold are enclosed in the gray shaded area. The figure displays only orderings up to 55 meV atom^{-1}.

this work, which were computed at 0 K, excluding any entropic or pV effects not explicitly accounted for in these simulations. We find that a significant number of structural orderings (i.e., 142) fall below the 30 meV atom^{-1} threshold, including ≈111 bulk orderings and ≈31 stacking faults models. This result suggests a rich, experimentally accessible configurational landscape for the arrangement of cation species, as well as a complex LYC structure containing both bulk-like and stacking fault features. The thermodynamic stability of each structural model in Figure 5 is directly influenced by the distribution of Y/Li cations among the octahedral sites formed by the Cl anion framework. Only specific Y/Li orderings minimize the electrostatic repulsion between Y^{3+} and Li^+ ions and correspond to those with a low energy above the convex hull. Notably, the low energy structures in Figure 5 feature Li face-sharing chains, in excellent agreement with previous observations by Schlem et al.[55] In general, the Y ordering in LYC has a significant impact on the relative stability of each structural model, while the energetics of our models are less dependent on the Li ordering. This observation is in agreement with the minimal 6g/6h site preference previously observed by Schlem et al.,[55] our DFT results reinforce the idea that Li is expected to be extremely mobile in LYC.

Our calculations on bulk structures of Li_3YCl_6 indicate that low energy structures, i.e., with energies above the convex hull below 25 meV atom^{-1}, never display face-sharing YCl_6^{3-} octahedra. Yet, some higher energy structures (both stacking fault and bulk models) below the 30 meV atom^{-1} threshold do include face-sharing YCl_6^{3-} octahedra and are likely accessible via mechanochemical synthesis. Therefore, the formation of stacking faults among other stable bulk configurations in LYC is expected after ball milling.

2.4. Probing Li and Y Local Environments with NMR.

Having recognized the presence of stacking faults through diffraction and DFT simulations, the Li and Y local environments in the BM-LYC and SS-LYC samples were investigated using solid-state NMR spectroscopy. Notably, NMR is a local structure technique and is therefore a powerful
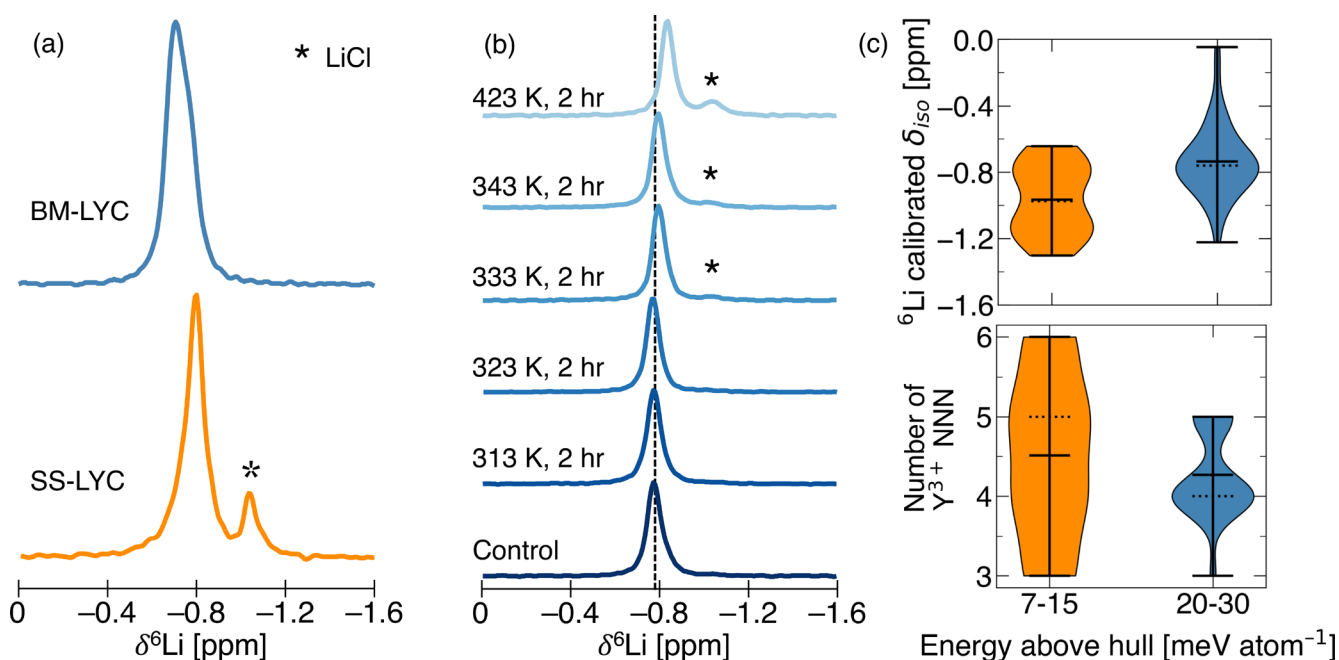
Figure 6. (a) ^{6}Li NMR spectra for as-prepared BM-LYC and SS-LYC. (b) ^{6}Li NMR spectra collected on a series of BM-LYC samples heat treated at various temperatures from room temperature to 423 K (150 °C). Besides the control sample which was only sealed in a capillary, all samples were heated in a sealed capillary for a period of ≈2 h. LiCl is labeled with an asterisk (∗). All spectra were acquired at 18.8 T with a spinning speed of 25 kHz and a set temperature of 298 K. (c) Distribution of DFT-calculated ^{6}Li isotropic chemical shifts and number of Y^{3+} next nearest neighbors (NNN) for Li atoms in enumerated LYC orderings grouped according to their energy above the convex hull from Figure 5. The lowest energy LYC ordering was ≈7 meV atom^{-1} above the hull. Computed structures included some instances of YCl_6^{3-} face-sharing octahedra. The solid and dotted horizontal bars inside the shaded areas represent the mean and median values, respectively.

probe of the phases present in samples regardless of their degree of crystallinity. Since the presence of (1/3, 2/3) Y layer faults yields different local environments for the Y atoms near the faulted layer (see Figure 3e), ^{89}Y NMR can be used to differentiate between LYC phases with varying amounts of such faults. Simultaneously, ^{6}Li NMR provides high-resolution insight into the Li substructure.

The differences in the Li substructures between samples prepared via ball milling or solid-state synthesis were first explored, and the ^{6}Li NMR spectra of the two samples are presented in Figure 6a. The main ^{6}Li signal for SS-LYC is centered at approximately −0.82 ppm and clearly resolved from its LiCl impurity peak at approximately −1.05 ppm. A single resonance is observed in the spectrum collected on BM-LYC and is centered at approximately −0.70 ppm, which is offset to more positive ppm values relative to the solid-state sample. The BM-LYC ^{6}Li NMR line shape is broader and less symmetrical than that of its solid-state counterpart, suggesting that it is composed of several overlapping signals with very similar resonant frequencies due to a distribution of Li environments in the more disordered BM-LYC structure.

The decrease in the amount of stacking faults and defect layers upon heating, as observed via diffraction (see Figure 4d), warrants an NMR-based investigation of the effect of heat treatments on the Li substructure. Capillaries containing BM-LYC powder samples were sealed, held for ≈2 h at various temperatures up to 423 K (150 °C), and air quenched to characterize the temperature-induced structural evolution. The ^{6}Li NMR spectra obtained at room temperature on these samples are plotted in Figure 6b. A control sample that was sealed in a capillary but not heat treated was also measured to ensure that any effects from flame-sealing could also be

accounted for. With increasing temperature, the ^{6}Li line shape shifts to more negative ppm values and approaches the isotropic shift of the SS-LYC sample. Starting at 333 K (60 °C), a LiCl component appears and continues to grow at higher temperatures, suggesting that the evolution of the BM-LYC disordered structure is linked to the presence of LiCl.

DFT calculations of ^{6}Li NMR parameters were performed on enumerated bulk structures considered for the analysis of structural energetics (Figure 5) to elucidate the origin of the temperature-dependent ^{6}Li shift of BM-LYC. Figure 6c depicts the distributions of calculated ^{6}Li shift values (^{6}Li shift calibration provided in section S5) and of the number of Y^{3+} next nearest neighbors (NNN) to Li atoms in selected structural models, which are grouped according to their energy above the convex hull. Two groupings are considered: the first comprises the low energy structures with energies ranging between ≈7 and 15 meV atom^{-1} (see Figure 8), while the higher energy bin corresponds to structures with energies between ≈20 and 30 meV atom^{-1} and contains instances of YCl_6^{3-} face-sharing octahedra. Full stacking fault structures, which contain more formula units per unit cell, were not calculated due to prohibitively high computational cost. While structures in the 20−30 meV atom^{-1} range (blue bin in Figure 6c) have shifts that are mostly centered near approximately −0.75 ppm, ^{6}Li shifts for the lower energy structures are found to have more negative chemical shifts, as evidenced by the inferior mean and median values. When the number of Y^{3+} NNN to each Li atom is considered, it can be seen that the more negative chemical shift of the low energy structures is correlated with a greater number of surrounding Y^{3+} ions.

Before any exposure to elevated temperatures, the BM-LYC sample can be thought of as consisting of structures in the 20−

30 meV atom^{-1} range, which include instances of face-sharing YCl_6^{3-} octahedra. However, the heat treatment provides enough thermal energy to enable structural rearrangements leading to lower energy configurations (approximately 7−15 meV atom^{-1}), as evidenced by the shifting of the average ^6Li resonance. This yields a more negative ^6Li chemical shift for the SS-LYC sample annealed at 823 K (550 °C) for multiple days. 330 K (60 °C) appears to be a threshold temperature for the stability of BM-LYC: above this temperature, the structure begins to evolve as demonstrated by the shift of the ^6Li resonances to more negative ppm values. Attributing the decreasing ^6Li chemical shift in BM-LYC to an increase in the number of Y^{3+} NNN to each Li atom is consistent with the elimination of Li-only defects, as observed from diffraction.

To facilitate the acquisition of ^{89}Y NMR data, Sm^{3+} was doped into the LYC structure, whereby the paramagnetic Sm^{3+} species replace some of the diamagnetic Y^{3+} ions in the nominal $Li_3Y_{0.95}Sm_{0.05}Cl_6$ composition (LYC-Sm) and trigger paramagnetic relaxation enhancements (PREs) that drastically shorten the ^{89}Y longitudinal (T_1) relaxation times. The shorter ^{89}Y NMR signal lifetime leads to a significant reduction in the recycle delay used between NMR scans, which enables the acquisition of ^{89}Y spectra with acceptable signal-to-noise ratio.[61] Notably, doping of paramagnetic Sm^{3+} into the LYC structure does not result in significant crystallographic differences (see XRD patterns in Figure S9) due to the similar ionic sizes of Y^{3+} (0.900 Å) and Sm^{3+} (0.958 Å) in octahedral environments.[62]

Figure 7a shows the ^{89}Y NMR spectra collected on the Sm-doped ball milled and solid-state LYC samples acquired at 298 K. The presence of 0.05 Sm^{3+} does not induce a paramagnetic shift for ^6Li or ^{89}Y but slightly broadens the ^6Li resonance relative to the undoped sample (see Figures S10 and S11). The ^{89}Y NMR signals observed in the spectra collected on the SS- and BM-LYC-Sm samples fall within the same ≈390 ppm to ≈460 ppm chemical shift range but have dissimilar lineshapes. The SS-LYC-Sm ^{89}Y spectrum is made up of four, clearly resolved resonances, centered at 386, 396, 410, and 421 ppm, respectively. A fit of the spectrum results in four peaks corresponding to 19%, 27%, 43%, and 11% of the total integrated ^{89}Y signal intensity (see Figure S12). In contrast, a single broad signal is observed in the BM-LYC-Sm ^{89}Y spectrum, which is presumably composed of closely spaced and overlapping resonances as expected for increased disorder and a distribution of Y environments in the material. Due to the difficulty in deconvoluting individual resonances, the BM-LYC ^{89}Y spectrum cannot be fitted reliably.

To assist the interpretation of the ^{89}Y NMR spectra, DFT calculations of ^{89}Y isotropic shifts in enumerated bulk LYC orderings with and without face-sharing between YCl_6^{3-} octahedra were conducted (see details in Computational Methods section). Results from these calculations are plotted in Figure 7b. A group of eight structures were computed (6 $Li_9Y_3Cl_{18}$ unit cells and 2 $Li_{18}Y_6Cl_{36}$ supercells) with every structure lying within ≈25.5 meV atom^{-1} from the hull. The calculated isotropic shifts were converted to experimentally relevant values using a calibration curve constructed from a range of reported ^{89}Y shifts for Y-containing compounds (see section S10 for calibration curve data and additional details). Structures are classified into two categories according to whether or not they contain face-sharing YCl_6^{3-} octahedra. For the structures that do not, all the NNN of Y^{3+} cations are
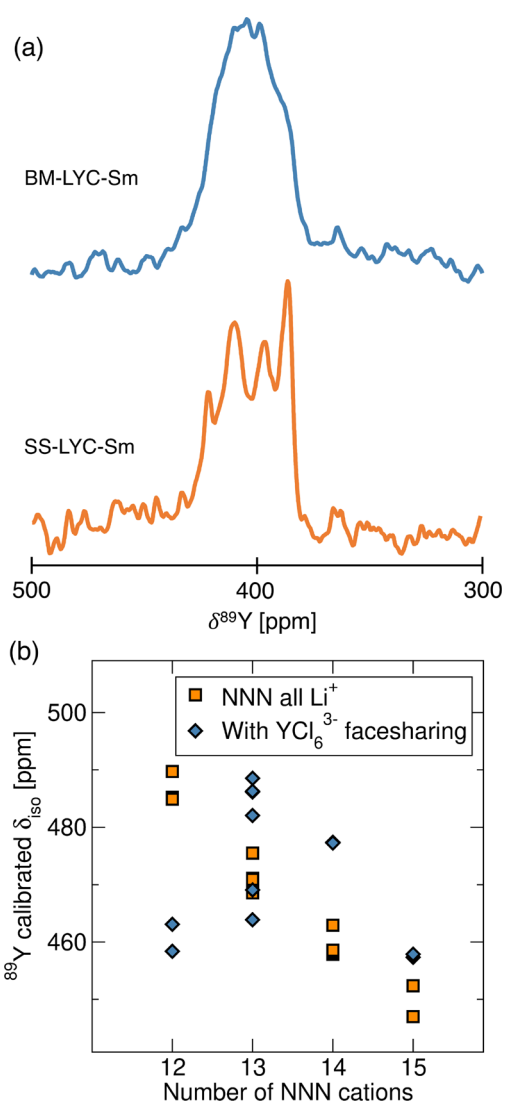

Figure 7. (a) ^{89}Y resonances for the Sm-doped LYC samples, BM-LYC-Sm and SS-LYC-Sm. All spectra were acquired at 18.8 T and a 10 kHz MAS rate with a set temperature of 298 K. (b) Isotropic ^{89}Y chemical shifts plotted as a function of the number of next nearest neighbor (NNN) cations for each corresponding Y^{3+}. The shifts were computed with DFT for bulk orderings within 25.5 meV atom^{-1} from the convex hull in Figure 5.

octahedral Li^+, mostly edge and corner sharing via Cl anions. The ^{89}Y chemical shifts corresponding to these environments fall into four clear ranges according to the number of Li^+ NNN, with more Li^+ neighbors resulting in a more negative shift value, which is consistent with previous reports on Y-containing aluminosilicate glasses.[63] The four computed chemical shift bins are reminiscent of the four signals observed in the ^{89}Y NMR spectrum of the SS-LYC-Sm compound in Figure 7a, suggesting that the NNN of Y^{3+} cations in the solid-state sample are almost all Li^+. The ppm differences between the average shift of each bin are calculated to be 15, 12, and 10 ppm, respectively, and agree remarkably well with the separations between the fitted peaks for the SS-LYC-Sm ^{89}Y spectrum of 10, 14, and 11 ppm. We note that comparisons between the computed and experimental shifts are based on relative ppm differences, rather than absolute values, as the calibration curves derived from first-principles can lead to a chemical shift offset.[64]
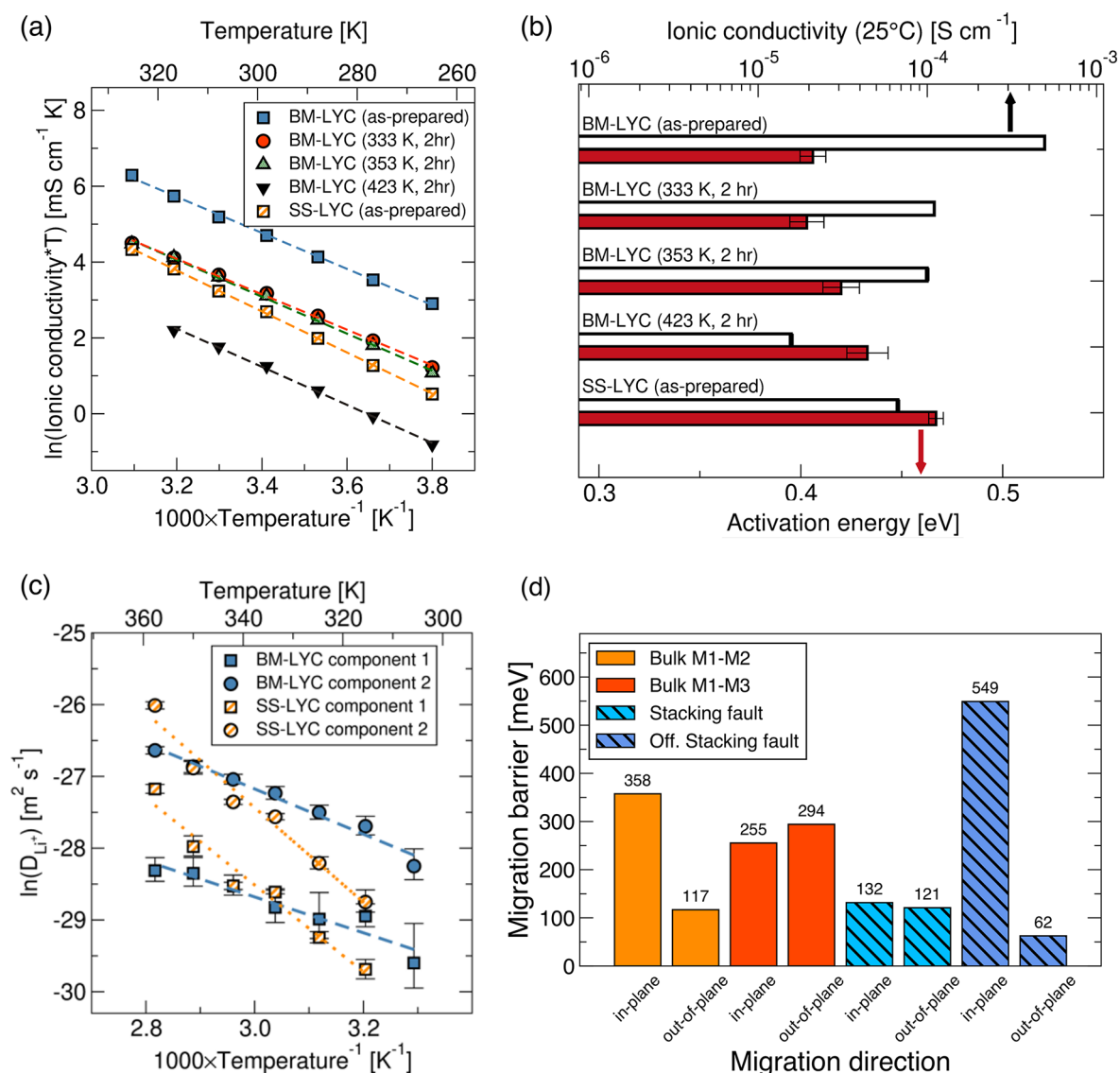
Figure 8. (a) Arrhenius behavior of EIS-measured ionic conductivity for as-prepared BM-LYC and heat treated samples (b) Room temperature ionic conductivity and activation energy for Li$^+$ long-range diffusion for various LYC samples. (c) Variable temperature PFG-NMR measurements on as-prepared BM- and SS-LYC samples. All measurements were conducted at 7.05 T. (d) Predicted migration barriers in (eV) for Li$^+$ ions in different model structures: bulk M1−M2 (orange bars), bulk M1−M3 (red bars), stacking fault (light blue), and off-stoichiometric stacking fault (blue). The uncertainty of the migration barriers is ±0.06 eV.[65] All error estimates are for one standard deviation.

Inclusion of structures containing face-sharing YCl_6^{3-} octahedra breaks the aforementioned binning as it leads to a broad chemical shift range for a given number of NNN Li$^+$. While some spectral broadening is to be expected for a mechanochemically synthesized sample due to a wider range of possible bond lengths and angles in the strained, defective structure, the lack of clear clusters of computed ^{89}Y chemical shifts is consistent with the broad NMR spectrum for BM-LYC-Sm. This observation is in agreement with the presence of face-sharing YCl_6^{3-} octahedra in BM-LYC, a key feature of our proposed stacking fault model.

2.5. Evaluation of Li$^+$ Ion Conduction Properties. The Li$^+$ ion conductivities and activation energies of a series of LYC samples were measured with electrochemical impedance spectroscopy (EIS). Representative Nyquist plots and fits are provided in Figure S14. Fits of the EIS data were performed using an equivalent circuit comprising a parallel resistor and a constant phase element (CPE), to capture the combined grain and grain boundary conduction, in series with a CPE to capture the electrodes' response. Measured conductivities therefore do not deconvolute grain and grain boundary contributions, providing instead a total conductivity through the LYC pellet.

Plots of the temperature dependence of the ionic conductivity, as well as of the room temperature conductivities and activation energies, are provided in Figure 8a,b. The measured ionic conductivity at 298 K (25 °C) (of 0.49 mS cm^{-1} and 0.067 mS cm^{-1}) and activation energy (of 0.41 ± 0.006 eV and 0.47 ± 0.004 eV) (all confidence intervals listed are 1σ) for the as-prepared BM-LYC and SS-LYC samples, respectively, are in good agreement with published values from Asano et al.[10] and Schlem et al.[31] The influence of metastable defects and of the Li substructure on Li$^+$ conduction in BM-LYC is probed by measuring the EIS response of samples heat treated under analogous conditions to the samples considered in Figure 6b. As shown in Figure 8b, the heat treatments at

333, 353, and 423 K decrease the room temperature ionic conductivity of the samples relative to the as-prepared compound. At temperatures higher than 333 K (60 °C), Li$^+$ diffusion barriers increase, suggesting that the evolution of the BM-LYC structure above 333 K affects Li$^+$ conduction pathways. While previous experiments by Schlem et al.[31] tested 5 min and 1 h of annealing at 823 K (550 °C), the temperatures tested here are far lower, emphasizing the facile tunability of BM-LYC's Li$^+$ conductivity upon exposure to moderate temperatures.

Variable temperature ^{7}Li PFG-NMR measurements on BM- and SS-LYC are shown in Figure 8c. PFG-NMR tracks the self-diffusion of ^{7}Li nuclei (D_{Li}^+) through a material by applying a magnetic field gradient across the height of the sample, giving spins a spatial encoding, and measuring their NMR signal after a time (Δ) during which the Li$^+$ ions diffuse. Relative to EIS, PFG-NMR probes short-range diffusion on the nm−μm length scale and can access intragrain conduction properties.[66] For BM-LYC, diffusion constants could be measured down to ≈304 K on account of its superior diffusion at relatively low temperatures. In both LYC samples, two diffusing components are observed that can be attributed to Li$^+$ ion conduction within LYC particles. All measured self-diffusion constants are tabulated in Table S5.

The derived activation energies for ion migration in BM-LYC are 0.25 ± 0.01 eV and 0.18 ± 0.03 eV (all confidence intervals listed are 1σ) for components 1 and 2, respectively. For SS-LYC, these are 0.57 ± 0.09 eV and 0.48 ± 0.1 eV. The measured activation energies of SS-LYC are comparable to the 0.47 eV EIS-measured value, while the values for BM-LYC are much lower than the measured 0.41 eV. Because the temperature range probed in our PFG-NMR measurements extends up to 363 K (90 °C), which is higher than the critical temperature of 333 K (60 °C) above which the long-range Li$^+$ conductivity of BM-LYC decreases, the measured activation energies for BM-LYC should be considered as lower bounds.

Variable diffusion time (Δ) PFG-NMR measurements were also conducted to check for impeded transport across grain boundaries, and the results are displayed in Figure S15. The diffusion length for a migrating spin is given by $r = (6D\Delta)^{1/2}$. Hence, monitoring self-diffusion constants as a function of the applied Δ and comparing the diffusion length with the average grain size of a sample can provide information about the relative ease of intragrain vs intergrain diffusion processes. No change in the D_{Li}^+ is observed for SS-LYC as the Δ time is increased, while BM-LYC D_{Li}^+ values monotonically decrease with increasing Δ. This behavior is consistent with impeded conduction across grain boundaries, i.e., as the diffusion length scale exceeds the BM-LYC average grain size but cannot be deconvoluted from potential effects from heating at 363 K (90 °C). In fact, the larger errors in the D_{Li}^+ values for the BM-LYC sample may be caused by structural evolution from heating or by a distribution of spin−spin relaxation times (T_2) due to the presence of a wide range of ^{7}Li environments. SEM images as well as D_{Li}^+ values and length scales can be found in the Supporting Information (Table S6, Figure S16).

To better understand the impact of stacking faults on the Li$^+$ conduction pathways, bond valence maps were calculated on four model LYC structures with varying Li/Y site occupations and defect layers. Bond valence maps are 3D potential maps for the diffusing Li$^+$ ions. They are determined by the bond valence site energy (BVSE) method and provide insight into

how Li$^+$ ions migrate through a crystal structure.[67,68] Of the four structures analyzed, two are free of stacking faults and correspond to an M1−M2 configuration (i.e., equal Y occupation of 1a and z = 0.5 2d sites) and an M1−M3 configuration (i.e., Y only in 1a and z = 0 2d sites), respectively.[31] In the M1−M2 model (Figure S17), Li$^+$ conduction occurs primarily along the c-axis, emphasizing facile Li$^+$ migration along O$_h$−O$_h$ paths between face-sharing octahedra, as predicted by Wang et al.[18] The M1−M3 structure (Figure S18), while retaining the preferential c-axis diffusion, displays increased ab-plane connectivity as the Y-free z = 0.5 layer provides greatly decreased Coulombic repulsion between Li$^+$ and Y^{3+} ions. Bond valence maps for two additional faulted structural models obtained from fits of the X-ray patterns in Figure 4 were also computed and reveal new site linkages. The first of these structures contains only (1/3, 2/3) Y layer faults and is illustrated in Figure S19. While face-sharing YCl$_6^{3-}$ octahedra decrease the Li site connectivity in their vicinity due to strong Coulombic repulsion with migrating Li$^+$ ions, they lead to regions of enhanced Li site connectivity elsewhere through the appearance of "loop" connectivity features, which bridge four neighboring Li sites across the ab plane and c axis. An additional structure that includes both Y (1/3, 2/3) faults, as well as the Y-free Li defect layers (Figure S20), illustrates how both faults work in tandem to further increase Li site connectivity, as the loop features appear alongside the linked Li sites of the Li defect layer along the ab-plane. Altogether, bond valence maps of faulted structures highlight how the presence of defects can locally increase the degree of Li site connectivity, which provides an intuitive explanation for the improvement in Li$^+$ conductivity upon ball milling.

First-principles calculations were carried out to assess the transport of Li$^+$ ions in bulk LYC models and in the vicinity of planar defects.[18] Li$^+$ migration barriers are influenced by the presence of Y and other Li$^+$ in the vicinity of the migrating ion. Given the large number of possible Li/Y orderings and stacking fault models for LYC (see Figure 5), the number of migration barriers to be considered can easily grow exponentially. Here, we only compute the Li$^+$ migration barriers in the same structural models used for bond valence mapping and along different crystallographic directions. The results of these calculations are presented in Figure 8d. The migration barriers were computed with DFT (at the SCAN level of theory) and using the nudged elastic band (NEB) method (see Computational Methods section).[69] The accuracy of the migration barriers in Figure 8d is estimated to be ±0.06 eV,[65] which approximately matches 1 order of magnitude in diffusivity.

Macroscopic Li transport is enabled by a percolation network of Li$^+$ migration pathways in the particles of LYC. Two distinct migration paths can result in Li percolation in LYC, nominally, (i) 2D Li$^+$ migration in the ab plane between octahedral sites bridged by a tetrahedral site (these pathways are referred as in-plane) and (ii) Li$^+$ migration perpendicular to the 2D layers of Li (along the crystallographic direction c) and termed out-of-plane (see Figure 1). This anisotropic diffusion mechanism has been previously reported for LYC and other layered Li$_3$MX$_6$ compositions.[10,18,70]

Stoichiometric LYC contains intrinsic vacancies on the Li sublattice, which actively participate in Li$^+$ migration. In Figure 8d, the Li$^+$ migration barriers for the M1−M2 and M1−M3 bulk models as well as the stoichiometric stacking fault model

use the existing vacancy network without removing a Li atom. In contrast, for the off-stoichiometric fault model, all of the Li sites in the Li-only defect layer are filled so a vacancy was introduced in the structure to enable ion migration.

The results shown in Figure 8d indicate that the lowest energy M1−M2 bulk ordering ($\approx$7.56 meV atom^{-1} above the hull) leads to in-plane and out-of-plane computed barriers of 0.358 and 0.117 eV, respectively. The M1−M3 bulk ordering ($\approx$9.8 meV atom^{-1} above the hull) results in in-plane and out-of-plane barriers of 0.255 and 0.294 eV, respectively. The stacking fault model with the lowest energy above the convex hull ($\approx$24.10 meV atom^{-1} above the hull) with the Li_3YCl_6 stoichiometry leads to in-plane and out-of-plane barriers of 0.132 and 0.121 eV, respectively. The model for an off-stoichiometric stacking fault results in in-plane and out-of-plane barriers of 0.549 and 0.62 eV, respectively.

From Figure 8d, one notices a large variability in the migration barriers derived for the different bulk or stacking fault models. In general, the migration barriers of in-plane pathways are larger than those of out-of-plane pathways. An exception to this trend is the set of barriers computed for the M1−M3 model. The lowest computed barrier is that of Li migrating out-of-plane in the off-stoichiometric fault. In fact, the out-of-plane Li$^+$ migration barriers are consistently lower in the stacking fault models than in the bulk models (i.e., M1−M2 and M1−M3). These results suggest that stacking faults are key to facile Li transport in LYC.

3. DISCUSSION

The results presented above emphasize the complexity of the defect landscape in LYC and its role in promoting Li$^+$ conduction through the structure. While previous literature had exclusively reported Y^{3+} site-disorder, our work demonstrates that mechanochemical synthesis of LYC can cause the coexistence of stacking faults and Li-only defect layers, as evidenced by a combination of high resolution synchrotron X-ray diffraction data, NMR, and DFT. These defects are metastable, allowing for a highly tunable conductivity. When ball milled samples are exposed to temperatures above 333 K (60 °C), the defect concentration decreases and Li$^+$ conduction is reduced.

Examining the Li$^+$ transport properties of LYC with the combination of EIS and PFG-NMR probes migration of Li$^+$. The two diffusing components observed with PFG-NMR (Figure 8c) likely correspond to in-/out-of-plane diffusion. Since c-axis conduction usually has a lower migration barrier, component 1 is assigned to diffusion along the c-axis and component 2 to ab-plane diffusion. For the ball milled sample, both components exhibit much lower activation energies than that of bulk Li$^+$ conduction measured by EIS (0.25 $\pm$ 0.01 eV and 0.18 $\pm$ 0.03 eV vs 0.41 $\pm$ 0.006 eV), reflecting that Li$^+$ conduction within individual particles is more facile than across grain boundaries and likely enhanced by the high concentration of defects within each particle. NEB calculations informed by bond valence maps show that stacking faults and Li defect layers generate additional site linkages with lower migration barriers and facilitate Li$^+$ ion transport. These defects create areas of dense Y^{3+} cation distribution (i.e., Y face-sharing moieties) and other areas of sparse Y^{3+} distribution, where migrating Li$^+$ ions experience less repulsive forces from nearby Y^{3+} ions. Among the Li_3MX_6 family of compounds, sparser M^{3+} distributions have been reported to improve Li$^+$ conduction and are a critical parameter for

designing better halide Li-ion solid electrolytes.[71] While intraparticle conduction is facilitated by defects, grain boundaries still hinder long-range Li$^+$ conduction, as evidenced by both the decreasing Li$^+$ self-diffusion constants at longer Δ values from PFG-NMR and the high activation energy from EIS for bulk migration.

Previous computational investigations of Li$^+$ migration in LYC have mostly relied on *ab initio* molecular dynamic simulations (AIMD)[18] and are often limited to a single Li/Y ordering in the bulk structure and specific direction for Li$^+$ migration. Undoubtedly, AIMD provides appealing results that are directly "comparable" with experimental EIS measurements. However, our NEB calculations are advantageous as they isolate favorable mechanisms of Li$^+$ migration and link Li$^+$ transport directly to the underlying structural motif, information often lost in the collective nature of AIMD simulations. In general, our computed migration barriers agree well with previous computational data.[18,71] Using AIMD on a M1−M2-bulk configuration, Wang et al.[18] derived an average migration barrier of $\approx$0.19 $\pm$ 0.03 eV, which is in agreement with our findings for out-of-plane diffusion. In contrast, they reported a much smaller barrier ($\approx$0.23 $\pm$ 0 0.06 eV) (all confidence intervals listed are 1σ) for the in-plane Li$^+$ migration pathway ($\approx$0.358 eV in this work). Furthermore, Wang et al.[18] showed that introducing one and three antisite defects between Li$^+$ and Y^{3+} yields an average activation energy of 0.28 $\pm$ 0.03 eV and 0.31 $\pm$ 0.03 eV, respectively. Similarly, Kim et al.,[71] who included explicit van der Waals corrections in their AIMD simulation, obtained a larger average Li$^+$ migration activation energy of $\approx$0.370 eV. While the existing data are in agreement with our results of Figure 8d, by explicitly considering the occurrence of stacking faults in the LYC structure, our simulations go beyond the analysis of Li$^+$ migration in pristine bulk structures, which cannot reflect the defect-rich mechanochemically synthesized structures. Further, the use of local experimental and computational tools in this work is justified by the strong dependence of the LYC short-range structure and Li$^+$ mobility on the synthesis protocol. In turn, our results enable us to provide microscopic insights into previous computational and experimental observations on halide solid electrolytes.

While Schlem et al.[31] had reported significant changes in the site disorder of LYC for very short times of annealing at 823 K (550 °C), here, we show that the defect concentration begins to decrease at $\approx$333 K (60 °C), leading to a lower ionic conductivity as determined from EIS. Variable temperature synchrotron XRD and NMR measurements on heat treated samples indicate the elimination of Li$^+$ defect layers and concurrent generation of LiCl. LiCl, being far less conductive, likely confines some of the Li$^+$ and prevents it from contributing to bulk conduction. The nonstoichiometry of LYC implied by the presence of Li-only defect layers is likely due to the fact that YCl$_3$ sticks to the agate mortar used for precursor mixing, a phenomenon also reported by Schlem et al.[31] The emergence of LiCl upon heating has also been reported for Li_3YbCl_6,[28] suggesting that nonstoichiometry and Li-defect layers could be present in other Li_3MCl_6 compositions. Stacking faults also appear to be eliminated at higher temperatures, although the exact mechanism is yet unknown. We speculate that stacking faults could be eliminated either through Y^{3+} migration, individual layer slippage that removes facesharing between YCl$_6{}^{3-}$ octahedra, or through grain growth, which consumes smaller, faulted

particles in favor of new unfaulted shells on larger pre-existing particles. Answering this question will be the subject of future investigations.

Although this is the first experimental investigation of stacking faults among Li_3MX_6 structures, it is likely that other kindred compositions are prone to similar stacking faults. The small energy difference between alternate stacking sequences for YCl_3,[52] and its similarity to the LYC crystal structure, serves as a possible explanation for the susceptibility of this class of materials to stacking faults. Given the similarities between the crystal structures of YCl_3 and other MCl_3 compounds (M = Yb, Er), as well as their tendency to form trigonal Li_3MCl_6, it is likely that Li_3YbCl_6 and Li_3ErCl_6 are susceptible to stacking faults when made via mechanochemical synthesis. Furthermore, evidence from Deng et al.[52] suggests that layered structures are favorable for larger halide anions as well and that alternate stacking sequences remain relatively close in energies. As such, Li_3MX_6 compositions where X = Br or I may also be prone to stacking faults. While these have yet to be reported, a computational investigation by Xu et al.[70] on the possible stacking sequences of Li_3LaI_6 has demonstrated that alternate stacking sequences result in energetically similar structures. Therefore, stacking fault formation is likely and could occur during mechanochemical synthesis. Future work on the family of Li_3MX_6 compounds should take care to ensure that potential stacking faults are accounted for in crystallographic analysis, and seek to better understand stacking fault susceptibility according to the identity of the alkali ion, anion, metal species.

In order to be used in commercially viable devices, solid electrolytes must maintain their conduction properties over a range of temperatures. The metastability of the planar defects that facilitate Li^+ conduction in LYC limits its range of applications as its ionic conductivity decreases markedly above 333 K (60 °C). Further investigation into strategies for stabilizing these defects and a better understanding of the factors that control their creation during synthesis are required to commercialize halide solid electrolytes.

4. CONCLUSION

A high concentration of stacking faults and other defects are identified in mechanochemically synthesized LYC and tied to its Li^+ conductive properties. Harnessing synchrotron X-ray diffraction, we have shown that that the as-made BM-LYC exhibits stacking faults that generate face-sharing YCl_6^{3-} octahedra. The BM-LYC is also suspected to have lithium rich layers within the material, suggesting a slight degree of off-stoichiometry. Cryo-TEM observations of domains containing stacking faults in the SS-LYC sample provide unquestionable evidence of the LYC layered structure's susceptibility to these planar defects. DFT calculations confirm that the observed defects are within the realm of entropically stabilized configurations at room temperature. Variable temperature diffraction and ^6Li and ^{89}Y solid-state NMR reveal that heat treatments, even at temperatures as low as 333 K (60 °C), reduce the concentration of defects in the material. Our PFG-NMR and EIS measurements, probing local and macroscopic Li^+ conduction, show that the defect concentration is intimately tied to the ionic conductivity of LYC; decreasing defect concentration via low temperature heat treatments is a means of tuning the ionic conductivity. Bond valence maps reveal new Li site linkages in the vicinity of planar defects as the locally sparse Y^{3+} distribution decreases the repulsive forces

experienced by migrating Li^+. Furthermore, NEB calculations confirm that these defects facilitate ionic conduction by lowering the Li^+ migration energy barrier. While these results constitute the first investigation of stacking faults among the ternary Li metal halides, we expect other kindred compositions may suffer from these faults. As such, future studies of these compounds must account for their presence and seek to better understand their formation.

5. EXPERIMENTAL SECTION

5.1. Materials Synthesis. All samples were synthesized under an inert Ar atmosphere. LiCl (99+%, Aldrich Chemical Company) was dried in a vacuum oven at 225 °C under dynamic vacuum for 24 h to remove residual moisture before being transferred into the glovebox. YCl_3 (99.99% trace metals basis, anhydrous, Sigma-Aldrich) was used as received. Precursors were hand-ground together with an agate mortar and pestle for 20 min with a 10% weight excess of YCl_3 to compensate for preferential adhesion of YCl_3 to the surface of the mortar, in accordance with previous reports.[31] $SmCl_3$ was used to dope LYC with Sm^{3+} on the Y^{3+} site to trigger a paramagnetic relaxation enhancement (PRE) that made ^{89}Y NMR more tractable, analogous to the procedure used by Grey et al. when studying pyrocholores.[61] When doping with Sm, a stoichiometric amount of $SmCl_3$ (99.9% trace metals basis, anhydrous, Sigma-Aldrich) was added to the powder mixture before grinding. For the ball mill synthesis, 1.6 g of hand-mixed powder was loaded into a ≈45 mL ZrO_2 jar along with seven 10 mm and 14 5 mm Y-stabilized zirconia spherical grinding media and sealed under Ar. The powder was milled at 8.3 Hz (500 rpm) for a total of 297 cycles of 5 min milling followed by 15 min rest with a high energy planetary ball mill (Retsch PM 200). Every 99 cycles, the jar was opened under Ar and caked-on powder was scraped from the edges with a spatula. For the solid-state synthesis, ≈1.8 g of hand-mixed powder was pressed into four roughly equivalent 6 mm diameter pellets and flame-sealed in a fused quartz tube (10 cm long, 13 mm inner diameter) under vacuum. Ahead of the sealing, the fused quartz tube was dried in a vacuum oven at 225 °C under dynamic vacuum for 12 h. The pellets were annealed at 550 °C for a total of 6 days in a tube furnace (Thermo Scientific Lindberg Blue M). To ensure a homogeneous final product, the pellets were removed from the tube, ground in an agate mortar, and repelletized after 2 days and 4 days of annealing.

To investigate structural evolution as a function of temperature, ball milled LYC was flame-sealed in capillaries and placed in a temperature-controlled environmental chamber (Tenney TJR-A-F4T). Capillaries were held there for 2 h before being removed and opened in the glovebox. Samples that were never exposed to elevated temperatures but were sealed in capillaries served as controls to prove the methodology did not lead to air or moisture exposure.

5.2. Diffraction. X-ray diffraction measurements were performed on ≈40 mg and ≈50 mg samples of ball milled and solid-state prepared Li_3YCl_6 powders, respectively, at beamline 17-BM at the Advanced Photon Source at Argonne National Laboratory. The temperature of the capillary samples was achieved using an Oxford Cryosystems Cryostream 800. Scattered intensity was measured by a PerkinElmer amorphous-Si flat panel detector. The wavelength for the measurements was 0.241 17 Å. Samples were measured first at 303 K, then at specific temperatures on heating up to 500 K. The heating rate was ≈1 K/min. The ball milled sample was also measured at 500 K after being held at that temperature for 50 min. Data were analyzed using the FAULTS program[72] (based on DIFFaX[73]) within the FullProf software suite.[74] The TOPAS software suite was used to show how the Rietveld refinement treatment of these data sets is inappropriate.[75]

Neutron diffraction measurements were performed on ≈1.2 g and ≈1.3 g samples of ball milled and solid-state prepared Li_3YCl_6 powders, respectively, at the National Institute of Standards and Technology Center for Neutron Research (NCNR). Data were collected at the high-resolution neutron powder diffractometer, BT-1, utilizing a Cu(311) monochromator with an in-pile 60′ collimator,

corresponding to a neutron wavelength of 1.5400 Å. Each sample was loaded into a vanadium sample can in a He environment glovebox and sealed with a soldered lead O-ring onto copper heating block. After mounting each sample onto a bottom-loaded closed cycle refrigerator (CCR), the same was measured at 303 K for a sufficient time so as to have appropriate data statistics. Data were analyzed using the FAULTS program[72] (based on DIFFaX[73]) within the FullProf software suite.[74]

5.3. Transmission Electron Microscopy. LYC samples were studied by cryo-TEM on a Titan 80-300 scanning/transmission electron microscope (S/TEM) operated at 300 kV. Particles were dispersed onto a TEM lacey carbon grid inside an Ar-filled glovebox. The specimen was then taken out into an airtight container and immediately plunged into liquid nitrogen followed by transferring of the specimen onto a precooled cryo-TEM holder (Elsa, Gatan, USA) using a cryotransfer station to ensure the entire process occurred under a cryogenic environment, which keeps the specimen in its native state. Then, the cryo-TEM holder was inserted into the TEM column for characterization at low temperature (100 K).

5.4. NMR. All one-dimensional spectra were acquired at 18.8 T (800 MHz for ^{1}H) on a Bruker Ultrashield Plus standard bore magnet equipped with an Avance III console. ^{6}Li measurements were done on a 2.5 mm HX MAS probe with 2.5 mm single cap zirconia rotors packed and closed with a Vespel cap under Ar with a PTFE spacer between the sample and cap to further protect the sample from air exposure. A flow of N$_2$ gas at 2000 L h^{-1} was used to control the rotor temperature and protect the sample from moisture contamination. Rotors were spun at 25 kHz using dry nitrogen, and data were obtained using a rotor synchronized spin–echo pulse sequence (90°-TR-180°-TR-ACQ). 90° and 180° flip angles of 3.125 μs and 6.25 μs, respectively, at 200 W were used with a 60 s recycle delay between scans. ^{6}Li chemical shifts were referenced to a 1 mol/L LiCl liquid solution at 0 ppm. Pulse lengths were calibrated on the same solution. All spectra were processed with Topspin 3.6 using 25 Hz of line broadening and identical phasing parameters.

^{89}Y measurements were done on a 3.2 mm HX MAS probe with 3.2 mm single cap sapphire rotors packed in the same way, spinning at 10 kHz under dry nitrogen. Due to the very long T_1 relaxation times of ^{89}Y, a previous acquisition on undoped LYC had a very poor signal-to-noise ratio after 24 h of measurements with a 300 s recycle delay. Sm^{3+} doping drastically reduced the T_1, allowing measurements to be acquired with a 120 s recycle delay. Spectra were referenced to 1 M YCl$_3$ at 0 ppm. Pulse lengths were calibrated on the solution. Direct excitation was done with a single pulse experiment using a flip angle of 40° corresponding to a 6 μs pulse at 100 W. All spectra were processed with Topspin 3.6 using 100 Hz of line broadening and identical phasing parameters.

PFG-NMR measurements were acquired at 7.05 T (300 MHz for ^{1}H) on a super wide bore Bruker magnet equipped with an Avance III console and using a Diff50 probe with a 10 mm ^{7}Li coil. Samples were loaded into 4 mm zirconia rotors and sealed under Ar inside of a 5 mm valved NMR tube. A continuous 800 L h^{-1} flow of N$_2$ gas over the NMR tube maintained an inert atmosphere throughout each measurement and also regulated the sample temperature. The exact temperature of the probe was calibrated using a dry ethylene glycol solution in the same configuration. ^{7}Li resonances were excited with 90° pulses of length 15.5 μs at 100 W and referenced to 1 M LiCl at 0 ppm. T_1 relaxation times at each temperature were determined with a saturation recovery; recycle delays for PFG measurements were set to 2.5T_1. PFG-NMR experiments were conducted with a variable magnetic field gradient sequence [maximum gradient of 0.28 T cm^{-1} (2800 G cm^{-1})] and a diffusion sequence with a stimulated echo to protect against transverse (T_2) relaxation. Gradient durations (δ), diffusion times (Δ), and gradient strengths were selected to guarantee an adequate decay curve. All measurements used the greatest allowable gradient strength to minimize values of δ and Δ and maximize the signal-to-noise ratio. δ and Δ times never surpassed 10 and 100 ms, respectively.

5.5. Scanning Electron Microscopy. High resolution images for ball milled and solid-state prepared LYC samples were obtained using a ThermoFisher Apreo C LoVac scanning electron microscope (SEM). Powdered samples were dispersed on top of carbon tape secured to a mounting stub. The samples were sealed under Ar until they were transferred inside the SEM, where vacuum was pulled immediately to minimize exposure to the atmosphere. The images were acquired under vacuum (below 10^{-5} mbar) using an accelerating voltage of 5 keV with 0.40 nA of current at a working distance of 9.7 mm. Backscattered and secondary electrons were detected with an Everhart–Thornley detector (ETD).

5.6. Computational Methods. We investigate the disorder of Li and Y in the Li$_3$YCl$_6$ structure using DFT,[76] where the exchange and correlation term was approximated by the strongly constrained and appropriately normed (SCAN) functional,[77] as implemented in the Vienna ab initio simulation package VASP code.[78,78] In VASP, the wave functions are expanded in terms of plane-waves with an energy cutoff of 520 eV, whereas the core electrons were described by the projector augmented-wave (PAW) theory.[79] The PAW potentials were Li [1s^{2}2s^1], Y [4s^{2}4p^{6}5s^{2}4d^1], and Cl [3s^{2}3p^5]. Using a constant k-point density of 727 Å^{-1} across all calculations, the total energy was converged within 10^{-5} eV and the atomic forces and stresses were converged to within 10^{-2} eV Å^{-1} and 0.29 GPa. These parameters were employed to investigate both the Li/Y orderings in the bulk structure, the stacking fault models, as well as the Li$^+$ migration barriers.

The low vacancy limit model was used to study Li$^+$ migration in Li$_3$YCl$_6$ structure, where the barriers for the migration of an isolated Li-vacancy are evaluated based on the nudged elastic band (NEB) method[69,80] available in VASP. NEB forces are converged within 0.50 eV Å^{-1}, following the protocol developed by Chen et al.[65] The supercell models of Li$_3$YCl$_6$ used in NEB calculations introduced a minimum distance of ≈10 Å between the migrating Li$^+$ ions, which avoids any undesired image–image interaction. The introduction of Li vacancies to enable ion migration was compensated by a countercharge in the form of a jellium.

NMR parameters for ^{6,7}Li and ^{89}Y were calculated using the CASTEP.[81] The generalized gradient approximation by Perdew, Burke, and Ernzerhof[82] was employed to approximate the exchange–correlation term. All calculations were run with "on-the-fly" ultrasoft pseudopotentials as supplied by CASTEP. NMR calculations were run using the projector augmented-wave method (GIPAW).[83,84] The scalar-relativistic zeroth-order regular approximation (ZORA)[85] was used for relativistic effects. The procedure for each calculation followed an identical sequence of single-point energy convergence with respect to a plane-wave cutoff energy and k-point grid, followed by a geometry optimization using the Broyden–Fletcher–Goldfarb–Shanno (BFGS) algorithm without constraints on the lattice, atomic positions, or imposed symmetry and concluded with a convergence of the chemical shielding constants with respect to a new cutoff energy and k-point grid.

Convergence criteria were the following: for single-point energy calculations, energy convergence tolerance was 0.5 meV atom^{-1}; for geometry optimization, energy convergence tolerance was 0.02 meV atom^{-1}, maximum ionic force tolerance was 0.05 eV Å^{-1}, maximum ionic displacement tolerance was 0.001 Å, and maximum stress component tolerance was 0.1 GPa. For the NMR calculations, the isotropic chemical shielding constant convergence tolerance was 0.01 ppm for Li shifts and 0.5 ppm for Y shifts. Converged cutoff energies and k-point grids used for geometry optimization and NMR parameter calculations are tabulated in section S4 of the Supporting Information.

CASTEP-calculated isotropic chemical shielding constants were converted to experimentally relevant chemical shifts through a semiempirical linear regression according to eq 1,

$$\delta_{\mathrm{iso}} = \sigma_{\mathrm{ref}} - m\sigma_{\mathrm{iso}} \tag{1}$$

where δ_{iso} is the experimentally calibrated chemical shift, σ_{iso} is the computed isotropic chemical shielding constant, m is a scaling factor, and σ_{ref} is the computed isotropic chemical shielding constant of a reference compound. Calibration curves were constructed using a series of binary Li and Y-containing compounds, in a method

analogous to that reported by Sadoc et al. for ^{19}F.[86] Final calibration curves, computed binaries, and references for ^{6,7}Li and ^{89}Y shifts are reported in the Supporting Information (see sections S5 and S10).

5.7. Electrochemical Impedance Spectroscopy. Ionic conductivity measurements were carried out with AC impedance on a Solartron 1260A analyzer. Pellets of ≈90 mg of powder were uniaxially pressed for 15 min at 350 MPa to relative densities of 76–79% and loaded into a custom-design hermetically sealed cell with stainless steel electrodes and a PEEK housing. The cell was placed in a Tenney TJR environment chamber and maintained under 180 MPa of pressure throughout the measurements with a vice. Impedance spectra were collected with excitation voltages of 10–30 mV between 8 MHz and 100 Hz and at a series of temperatures from 263 to 313 K in 10 K increments. Fitting of EIS spectra was conducted with the ZView software package. Errors in the calculated conductivity and activation energy accounted for fitting, temperature, and thickness measurement errors.

■ ASSOCIATED CONTENT

ⓈⒾ Supporting Information

The Supporting Information is available free of charge at https://pubs.acs.org/doi/10.1021/jacs.1c11335.

Cryo-TEM images; stacking fault model construction, neutron diffraction patterns, high temperature SS-LYC X-ray diffraction patterns, fit for β-LYC; accuracy of exchange and correlation functional; converged k-point and planewave energy cutoffs for NMR calculations; ^{6}Li and ^{89}Y NMR calibration curves; ^{6}Li, ^{89}Y NMR and XRD on undoped and Sm-doped LYC; fit for SS-LYC ^{89}Y NMR spectrum; EIS spectra and fits; Li^{+} self-diffusion coefficients as measured by PFG-NMR; SEM images; variable diffusion time PFG-NMR; bond valence maps on pristine and faulted structures (PDF)

■ AUTHOR INFORMATION

Corresponding Authors

Pieremanuele Canepa − *Department of Materials Science and Engineering, National University of Singapore, 117575, Singapore; Department of Chemical and Biomolecular Engineering, National University of Singapore, 117585, Singapore;* ⓘ orcid.org/0000-0002-5168-9253; Email: pcanepa@nus.edu.sg

Raphaële J. Clément − *Materials Department, University of California, Santa Barbara, California 93106, United States; Materials Research Laboratory, University of California, Santa Barbara, California 93106, United States;* ⓘ orcid.org/0000-0002-3611-1162; Email: rclement@ucsb.edu

Authors

Elias Sebti − *Materials Department, University of California, Santa Barbara, California 93106, United States; Materials Research Laboratory, University of California, Santa Barbara, California 93106, United States;* ⓘ orcid.org/0000-0003-2678-3536

Hayden A. Evans − *Center for Neutron Research, National Institute of Standards and Technology, Gaithersburg, Maryland 20899, United States;* ⓘ orcid.org/0000-0002-1331-4274

Hengning Chen − *Department of Materials Science and Engineering, National University of Singapore, 117575, Singapore*

Peter M. Richardson − *Materials Department, University of California, Santa Barbara, California 93106, United States;*

Materials Research Laboratory, University of California, Santa Barbara, California 93106, United States; ⓘ orcid.org/0000-0002-6631-2459

Kelly M. White − *Chemistry and Biochemistry Department and Materials Research Laboratory, University of California, Santa Barbara, California 93106, United States*

Raynald Giovine − *Materials Department, University of California, Santa Barbara, California 93106, United States; Materials Research Laboratory, University of California, Santa Barbara, California 93106, United States*

Krishna Prasad Koirala − *Physical and Computational Sciences Directorate, Pacific Northwest National Laboratory, Richland, Washington 99352, United States*

Yaobin Xu − *Environmental Molecular Sciences Laboratory, Pacific Northwest National Laboratory, Richland, Washington 99352, United States;* ⓘ orcid.org/0000-0002-9945-3514

Eliovardo Gonzalez-Correa − *Materials Department, University of California, Santa Barbara, California 93106, United States; Materials Research Laboratory, University of California, Santa Barbara, California 93106, United States*

Chongmin Wang − *Environmental Molecular Sciences Laboratory, Pacific Northwest National Laboratory, Richland, Washington 99352, United States;* ⓘ orcid.org/0000-0003-3327-0958

Craig M. Brown − *Center for Neutron Research, National Institute of Standards and Technology, Gaithersburg, Maryland 20899, United States;* ⓘ orcid.org/0000-0002-9637-9355

Anthony K. Cheetham − *Materials Department, University of California, Santa Barbara, California 93106, United States; Department of Materials Science and Engineering, National University of Singapore, 117575, Singapore; Materials Research Laboratory, University of California, Santa Barbara, California 93106, United States;* ⓘ orcid.org/0000-0003-1518-4845

Complete contact information is available at:
https://pubs.acs.org/10.1021/jacs.1c11335

Notes

The authors declare no competing financial interest.

■ ACKNOWLEDGMENTS

■ REFERENCES

(1) Janek, J.; Zeier, W. G. A Solid Future for Battery Development. *Nat. Energy* **2016**, *1*, 16141.

(2) Noi, K.; Nagata, Y.; Hakari, T.; Suzuki, K.; Yubuchi, S.; Ito, Y.; Sakuda, A.; Hayashi, A.; Tatsumisago, M. Oxide-Based Composite Electrolytes Using $Na_3Zr_2Si_2PO_{12}/Na_3PS_4$ Interfacial Ion Transfer. *ACS Appl. Mater. Interfaces* **2018**, *10*, 19605–19614.

(3) Jung, K.-N.; Shin, H.-S.; Park, M.-S.; Lee, J.-W. Solid-State Lithium Batteries: Bipolar Design, Fabrication, and Electrochemistry. *ChemElectroChem* **2019**, *6*, 3842–3859.

(4) Famprikis, T.; Canepa, P.; Dawson, J. A.; Islam, M. S.; Masquelier, C. Fundamentals of Inorganic Solid-State Electrolytes for Batteries. *Nat. Mater.* **2019**, *18*, 1278–1291.

(5) Groh, M. F.; Sullivan, M. J.; Gaultois, M. W.; Pecher, O.; Griffith, K. J.; Grey, C. P. Interface Instability in LiFePO$_4$–Li$_{3+x}$P$_{1-x}$Si$_x$O$_4$ All-Solid-State Batteries. *Chem. Mater.* **2018**, *30*, 5886–5895.

(6) Zhang, Z.; Zhang, L.; Liu, Y.; Yu, C.; Yan, X.; Xu, B.; Wang, L.-m. Synthesis and Characterization of Argyrodite Solid Electrolytes for All-Solid-State Li-ion Batteries. *J. Alloys Compd.* **2018**, *747*, 227–235.

(7) Griffith, K. J.; Wiaderek, K. M.; Cibin, G.; Marbella, L. E.; Grey, C. P. Niobium Tungsten Oxides for High-Rate Lithium-Ion Energy Storage. *Nature* **2018**, *559*, 556–563.

(8) Adeli, P.; Bazak, J. D.; Park, K. H.; Kochetkov, I.; Huq, A.; Goward, G. R.; Nazar, L. F. Boosting Solid-State Diffusivity and Conductivity in Lithium Superionic Argyrodites by Halide Substitution. *Angew. Chem., Int. Ed.* **2019**, *58*, 8681–8686.

(9) Schlenker, R.; Hansen, A.-L.; Senyshyn, A.; Zinkevich, T.; Knapp, M.; Hupfer, T.; Ehrenberg, H.; Indris, S. Structure and Diffusion Pathways in Li$_6$PS$_5$Cl Argyrodite from Neutron Diffraction, Pair-Distribution Function Analysis, and NMR. *Chem. Mater.* **2020**, *32*, 8420–8430.

(10) Asano, T.; Sakai, A.; Ouchi, S.; Sakaida, M.; Miyazaki, A.; Hasegawa, S. Solid Halide Electrolytes with High Lithium-Ion Conductivity for Application in 4 V Class Bulk-Type All-Solid-State Batteries. *Adv. Mater.* **2018**, *30*, 1803075.

(11) Li, X.; Liang, J.; Yang, X.; Adair, K. R.; Wang, C.; Zhao, F.; Sun, X. Progress and Perspectives on Halide Lithium Conductors for All-Solid-State Lithium Batteries. *Energy Environ. Sci.* **2020**, *13*, 1429–1461.

(12) Wang, Y.; Richards, W. D.; Ong, S. P.; Miara, L. J.; Kim, J. C.; Mo, Y.; Ceder, G. Design Principles for Solid-State Lithium Superionic Conductors. *Nat. Mater.* **2015**, *14*, 1026–1031.

(13) Nam, K.; Chun, H.; Hwang, J.; Han, B. First-Principles Design of Highly Functional Sulfide Electrolyte of $Li_{10-x}SnP_2S_{12-x}Cl_x$ for All Solid-State Li-Ion Battery Applications. *ACS Sustainable Chem. Eng.* **2020**, *8*, 3321–3327.

(14) Park, K. H.; Bai, Q.; Kim, D. H.; Oh, D. Y.; Zhu, Y.; Mo, Y.; Jung, Y. S. Design Strategies, Practical Considerations, and New Solution Processes of Sulfide Solid Electrolytes for All-Solid-State Batteries. *Adv. Energy Mater.* **2018**, *8*, 1800035.

(15) Chen, Y.; Rangasamy, E.; Liang, C.; An, K. Origin of High Li$^+$ Conduction in Doped $Li_7La_3Zr_2O_{12}$ Garnets. *Chem. Mater.* **2015**, *27*, 5491–5494.

(16) Ren, Y.; Chen, K.; Chen, R.; Liu, T.; Zhang, Y.; Nan, C.-W. Oxide Electrolytes for Lithium Batteries. *J. Am. Ceram. Soc.* **2015**, *98*, 3603–3623.

(17) He, X.; Zhu, Y.; Mo, Y. Origin of Fast Ion Diffusion in Super-Ionic Conductors. *Nat. Commun.* **2017**, *8*, 15893.

(18) Wang, S.; Bai, Q.; Nolan, A. M.; Liu, Y.; Gong, S.; Sun, Q.; Mo, Y. Lithium Chlorides and Bromides as Promising Solid-State Chemistries for Fast Ion Conductors with Good Electrochemical Stability. *Angew. Chem., Int. Ed.* **2019**, *58*, 8039–8043.

(19) Adelstein, N.; Wood, B. C. Role of Dynamically Frustrated Bond Disorder in a Li$^+$ Superionic Solid Electrolyte (Li_3InBr_6). *Chem. Mater.* **2016**, *28*, 7218–7231.

(20) Zevgolis, A.; Wood, B. C.; Mehmedović, Z.; Hall, A. T.; Alves, T. C.; Adelstein, N. Alloying Effects on Superionic Conductivity in Lithium Indium Halides for All-Solid-State Batteries. *APL Mater.* **2018**, *6*, 047903.

(21) Li, X.; Liang, J.; Adair, K. R.; Li, J.; Li, W.; Zhao, F.; Hu, Y.; Sham, T.-K.; Zhang, L.; Zhao, S.; Lu, S.; Huang, H.; Li, R.; Chen, N.; Sun, X. Origin of Superionic $Li_3Y_{1-x}In_xCl_6$ Halide Solid-Electrolytes with High Humidity Tolerance. *Nano Lett.* **2020**, *20*, 4384–4392.

(22) Wan, T. H.; Ciucci, F. Ab Initio Study of the Defect Chemistry and Substitutional Strategies for Highly Conductive Li_3YX_6 (X = F, Cl, Br, and I) Electrolyte for the Application of Solid-State Batteries. *ACS Appl. Energy Mater.* **2021**, *4*, 7930–7941.

(23) Liang, J.; Li, X.; Wang, S.; Adair, K. R.; Li, W.; Zhao, Y.; Wang, C.; Hu, Y.; Zhang, L.; Zhao, S.; Lu, S.; Huang, H.; Li, R.; Mo, Y.; Sun, X. Site-Occupation-Tuned Superionic Li_xScCl_{3+x} Halide Solid Electrolytes for All-Solid-State Batteries. *J. Am. Chem. Soc.* **2020**, *142*, 7012–7022.

(24) Park, K.-H.; Kaup, K.; Assoud, A.; Zhang, Q.; Wu, X.; Nazar, L. F. High Voltage Superionic Halide Solid Electrolytes for All-Solid-State Li-Ion Batteries. *ACS Energy Lett.* **2020**, *5*, 533–539.

(25) Park, J.; Han, D.; Kwak, H.; Han, Y.; Choi, Y. J.; Nam, K.-W.; Jung, Y. S. Heat Treatment Protocol for Modulating Ionic Conductivity via Structural Evolution of $Li_{3-x}Yb_{1-x}M_xCl_6$ (M = Hf^{4+}, Zr^{4+}) New Halide Superionic Conductors for All-Solid-State Batteries. *Chem. Eng. J.* **2021**, *425*, 130630.

(26) Wu, E. A.; et al. A Stable Cathode-Solid Electrolyte Composite for High-Voltage, Long-Cycle-Life Solid-State Sodium-Ion Batteries. *Nat. Commun.* **2021**, *12*, 1256.

(27) Schlem, R.; Banik, A.; Eckardt, M.; Zobel, M.; Zeier, W. G. Na$_{3-x}$Er$_{1-x}$Zr$_x$Cl$_6$—A Halide-Based Fast Sodium-Ion Conductor with Vacancy-Driven Ionic Transport. *ACS Appl. Energy Mater.* **2020**, *3*, 10164–10173.

(28) Kim, S. Y.; Kaup, K.; Park, K.-H.; Assoud, A.; Zhou, L.; Liu, J.; Wu, X.; Nazar, L. F. Lithium Ytterbium-Based Halide Solid Electrolytes for High Voltage All-Solid-State Batteries. *ACS Mater. Lett.* **2021**, *3*, 930–938.

(29) Liu, Z.; Ma, S.; Liu, J.; Xiong, S.; Ma, Y.; Chen, H. High Ionic Conductivity Achieved in $Li_3Y(Br_3Cl_3)$ Mixed Halide Solid Electrolyte via Promoted Diffusion Pathways and Enhanced Grain Boundary. *ACS Energy Lett.* **2021**, *6*, 298–304.

(30) Li, J.; Ma, C.; Chi, M.; Liang, C.; Dudney, N. J. Solid Electrolyte: The Key for High-Voltage Lithium Batteries. *Adv. Energy Mater.* **2015**, *5*, 1401408.

(31) Schlem, R.; Muy, S.; Prinz, N.; Banik, A.; Shao-Horn, Y.; Zobel, M.; Zeier, W. G. Mechanochemical Synthesis: A Tool to Tune Cation Site Disorder and Ionic Transport Properties of Li_3MCl_6 (M = Y, Er) Superionic Conductors. *Adv. Energy Mater.* **2020**, *10*, 1903719.

(32) Ito, H.; Shitara, K.; Wang, Y.; Fujii, K.; Yashima, M.; Goto, Y.; Moriyoshi, C.; Rosero-Navarro, N. C.; Miura, A.; Tadanaga, K. Kinetically Stabilized Cation Arrangement in $Li3YCl6$ Superionic Conductor during Solid-State Reaction. *Advanced Science* **2021**, *8*, 2101413.

(33) Tessier, C.; Haumesser, P. H.; Bernard, P.; Delmas, C. The Structure of $Ni(OH)_2$: From the Ideal Material to the Electrochemically Active One. *J. Electrochem. Soc.* **1999**, *146*, 2059.

(34) Scholz, T.; Schneider, C.; Eger, R.; Duppel, V.; Moudrakovski, I.; Schulz, A.; Nuss, J.; Lotsch, B. V. Phase Formation through Synthetic Control: Polymorphism in the Sodium-Ion Solid Electrolyte $Na_4P_2S_6$. *J. Mater. Chem. A* **2021**, *9*, 8692−8703.

(35) Croguennec, L.; Deniard, P.; Brec, R.; Lecerf, A. Nature of the Stacking Faults in Orthorhombic $LiMnO_2$. *J. Mater. Chem.* **1997**, *7*, 511−516.

(36) Croguennec, L.; Deniard, P.; Brec, R.; Caldes Ricos, M. T.; Brohan, L. High Resolution Electron Microscopy Evidence of Stacking Faults in $O-LiMnO_2$. *Mol. Cryst. Liq. Cryst. Sci. Technol., Sect. A* **1998**, *311*, 101−108.

(37) Boulineau, A.; Croguennec, L.; Delmas, C.; Weill, F. Reinvestigation of Li_2MnO_3 Structure: Electron Diffraction and High Resolution TEM. *Chem. Mater.* **2009**, *21*, 4216−4222.

(38) Boulineau, A.; Croguennec, L.; Delmas, C.; Weill, F. Structure of Li_2MnO_3 with Different Degrees of Defects. *Solid State Ionics* **2010**, *180*, 1652−1659.

(39) Boulineau, A.; Croguennec, L.; Delmas, C.; Weill, F. Thermal Stability of Li_2MnO_3: From Localized Defects to the Spinel Phase. *Dalton Trans* **2012**, *41*, 1574−1581.

(40) Paulsen, J. M.; Thomas, C. L.; Dahn, J. R. Layered Li-Mn-Oxide with the O2 Structure: A Cathode Material for Li-Ion Cells Which Does Not Convert to Spinel. *J. Electrochem. Soc.* **1999**, *146*, 3560−3565.

(41) Xia, X.; Dahn, J. R. $NaCrO_2$ Is a Fundamentally Safe Positive Electrode Material for Sodium-Ion Batteries with Liquid Electrolytes. *Electrochem. Solid-State Lett.* **2012**, *15*, A1.

(42) Serrano-Sevillano, J.; Casas-Cabanas, M.; Saracibar, A. Impact of Stacking Faults and Li Substitution in Li_xMnO_3 $(0 \leq x \leq 2)$ Structural Transformations upon Delithiation. *J. Phys. Chem. Lett.* **2021**, *12*, 7474−7481.

(43) Mortemard de Boisse, B.; Reynaud, M.; Ma, J.; Kikkawa, J.; Nishimura, S.-i.; Casas-Cabanas, M.; Delmas, C.; Okubo, M.; Yamada, A. Coulombic Self-Ordering upon Charging a Large-Capacity Layered Cathode Material for Rechargeable Batteries. *Nat. Commun.* **2019**, *10*, 2185.

(44) Serrano-Sevillano, J.; Reynaud, M.; Saracibar, A.; Altantzis, T.; Bals, S.; van Tendeloo, G.; Casas-Cabanas, M. Enhanced Electrochemical Performance of Li-rich Cathode Materials through Microstructural Control. *Phys. Chem. Chem. Phys.* **2018**, *20*, 23112−23122.

(45) Clément, R. J.; Middlemiss, D. S.; Seymour, I. D.; Ilott, A. J.; Grey, C. P. Insights into the Nature and Evolution upon Electrochemical Cycling of Planar Defects in the $\beta-NaMnO_2$ Na-Ion Battery Cathode: An NMR and First-Principles Density Functional Theory Approach. *Chem. Mater.* **2016**, *28*, 8228−8239.

(46) Yu, D. Y. W.; Yanagida, K.; Kato, Y.; Nakamura, H. Electrochemical Activities in Li_2MnO_3. *J. Electrochem. Soc.* **2009**, *156*, A417.

(47) Li, Q.; Yao, Z.; Lee, E.; Xu, Y.; Thackeray, M. M.; Wolverton, C.; Dravid, V. P.; Wu, J. Dynamic Imaging of Crystalline Defects in Lithium-Manganese Oxide Electrodes during Electrochemical Activation to High Voltage. *Nat. Commun.* **2019**, *10*, 1692.

(48) Matsunaga, T.; Komatsu, H.; Shimoda, K.; Minato, T.; Yonemura, M.; Kamiyama, T.; Kobayashi, S.; Kato, T.; Hirayama,

T.; Ikuhara, Y.; Arai, H.; Ukyo, Y.; Uchimoto, Y.; Ogumi, Z. Dependence of Structural Defects in Li_2MnO_3 on Synthesis Temperature. *Chem. Mater.* **2016**, *28*, 4143−4150.

(49) Li, Z.; Fu, J.-Y.; Feng, Y.; Dong, C.-K.; Liu, H.; Du, X.-W. A Silver Catalyst Activated by Stacking Faults for the Hydrogen Evolution Reaction. *Nat. Catal.* **2019**, *2*, 1107−1114.

(50) Nemudry, A.; Weiss, M.; Gainutdinov, I.; Boldyrev, V.; Schöllhorn, R. Room Temperature Electrochemical Redox Reactions of the Defect Perovskite $SrFeO_{2.5+x}$. *Chem. Mater.* **1998**, *10*, 2403−2411.

(51) Li, X.; Bianchini, F.; Wind, J.; Vajeeston, P.; Wragg, D.; Fjellvåg, H. P2 Type Layered Solid-State Electrolyte $Na_2Zn_2TeO_6$: Crystal Structure and Stacking Faults. *J. Electrochem. Soc.* **2019**, *166*, A3830−A3837.

(52) Deng, Z.; Wei, F.; Wu, Y.; Seshadri, R.; Cheetham, A. K.; Canepa, P. Understanding the Structural and Electronic Properties of Bismuth Trihalides and Related Compounds. *Inorg. Chem.* **2020**, *59*, 3377−3386.

(53) Gorai, P.; Famprikis, T.; Singh, B.; Stevanović, V.; Canepa, P. Devil Is in the Defects: Electronic Conductivity in Solid Electrolytes. *Chem. Mater.* **2021**, *33*, 7484−7498.

(54) Steiner, H.-J.; Lutz, H. D. Neue schnelle Ionenleiter vom Typ $M^I_3M^{III}Cl_6$ (M^I = Li, Na, Ag; M^{III} = In, Y). *Z. Anorg. Allg. Chem.* **1992**, *613*, 26−30.

(55) Schlem, R.; Banik, A.; Ohno, S.; Suard, E.; Zeier, W. G. Insights into the Lithium Sub-structure of Superionic Conductors Li_3YCl_6 and Li_3YBr_6. *Chem. Mater.* **2021**, *33*, 327−337.

(56) Berliner, R.; Werner, S. A. Effect of Stacking Faults on Diffraction: The Structure of Lithium Metal. *Phys. Rev. B* **1986**, *34*, 3586−3603.

(57) Whelan, M. J.; Hirsch, P. B. Electron Diffraction from Crystals Containing Stacking Faults: II. *Philosophical Magazine: A Journal of Theoretical Experimental and Applied Physics* **1957**, *2*, 1303−1324.

(58) Bian, B.; Yang, W.; Laughlin, D.; Lambeth, D. Stacking Faults and Their Effect on Magnetocrystalline Anisotropy in Co and Co-alloy Thin Films. *IEEE Trans. Magn.* **2001**, *37*, 1456−1458.

(59) Yamane, H.; Yamada, T. Effects of Stacking Fault on the Diffraction Intensities of $\beta-FeSi_2$. *J. Alloys Compd.* **2009**, *476*, 282−287.

(60) Ong, S. P.; Richards, W. D.; Jain, A.; Hautier, G.; Kocher, M.; Cholia, S.; Gunter, D.; Chevrier, V. L.; Persson, K. A.; Ceder, G. Python Materials Genomics (Pymatgen): A Robust, Open-Source Python Library for Materials Analysis. *Comput. Mater. Sci.* **2013**, *68*, 314−319.

(61) Grey, C. P.; Smith, M. E.; Cheetham, A. K.; Dobson, C. M.; Dupree, R. ^{89}Y Magic Angle Spinning NMR Study of Rare-Earth Pyrochlores: Paramagnetic Shifts in the Solid State. *J. Am. Chem. Soc.* **1990**, *112*, 4670−4675.

(62) Shannon, R. D.; Prewitt, C. T. Revised Values of Effective Ionic Radii. *Acta Crystallogr., Sect. B: Struct. Crystallogr. Cryst. Chem.* **1970**, *26*, 1046−1048.

(63) Jaworski, A.; Charpentier, T.; Stevensson, B.; Edén, M. Scandium and Yttrium Environments in Aluminosilicate Glasses Unveiled by $^{45}Sc/^{89}Y$ NMR Spectroscopy and DFT Calculations: What Structural Factors Dictate the Chemical Shifts? *J. Phys. Chem. C* **2017**, *121*, 18815−18829.

(64) Reader, S. W.; Mitchell, M. R.; Johnston, K. E.; Pickard, C. J.; Whittle, K. R.; Ashbrook, S. E. Cation Disorder in Pyrochlore Ceramics: ^{89}Y MAS NMR and First-Principles Calculations. *J. Phys. Chem. C* **2009**, *113*, 18874−18883.

(65) Chen, T.; Sai Gautam, G.; Canepa, P. Ionic Transport in Potential Coating Materials for Mg Batteries. *Chem. Mater.* **2019**, *31*, 8087−8099.

(66) Harm, S.; Hatz, A.-K.; Moudrakovski, I.; Eger, R.; Kuhn, A.; Hoch, C.; Lotsch, B. V. Lesson Learned from NMR: Characterization and Ionic Conductivity of LGPS-like Li_7SiPS_8. *Chem. Mater.* **2019**, *31*, 1280−1288.

(67) Adams, S.; Rao, R. P. High Power Lithium Ion Battery Materials by Computational Design. *Phys. Status Solidi A* **2011**, *208*, 1746−1753.

(68) Chen, H.; Adams, S. Bond Softness Sensitive Bond-Valence Parameters for Crystal Structure Plausibility Tests. *IUCrJ* **2017**, *4*, 614−625.

(69) Henkelman, G.; Uberuaga, B. P.; Jónsson, H. A Climbing Image Nudged Elastic Band Method for Finding Saddle Points and Minimum Energy Paths. *J. Chem. Phys.* **2000**, *113*, 9901−9904.

(70) Xu, Z.; Chen, X.; Liu, K.; Chen, R.; Zeng, X.; Zhu, H. Influence of Anion Charge on Li Ion Diffusion in a New Solid-State Electrolyte, Li_3LaI_6. *Chem. Mater.* **2019**, *31*, 7425−7433.

(71) Kim, K.; Park, D.; Jung, H.-G.; Chung, K. Y.; Shim, J. H.; Wood, B. C.; Yu, S. Material Design Strategy for Halide Solid Electrolytes Li_3MX_6 (X = Cl, Br, and I) for All-Solid-State High-Voltage Li-Ion Batteries. *Chem. Mater.* **2021**, *33*, 3669−3677.

(72) Casas-Cabanas, M.; Reynaud, M.; Rikarte, J.; Horbach, P.; Rodríguez-Carvajal, J. FAULTS: A Program for Refinement of Structures with Extended Defects. *J. Appl. Crystallogr.* **2016**, *49*, 2259−2269.

(73) Treacy, M. M. J.; Newsam, J. M.; Deem, M. W. A General Recursion Method for Calculating Diffracted Intensities from Crystals Containing Planar Faults. *Proc. R. Soc. London, Ser. A* **1991**, *433*, 499−520.

(74) Rodríguez-Carvajal, J. Recent Advances in Magnetic Structure Determination by Neutron Powder Diffraction. *Phys. B* **1993**, *192*, 55−69.

(75) Coelho, A. A. TOPAS and TOPAS-Academic: An Optimization Program Integrating Computer Algebra and Crystallographic Objects Written in C++. *J. Appl. Crystallogr.* **2018**, *51*, 210−218.

(76) Kohn, W.; Sham, L. J. Self-Consistent Equations Including Exchange and Correlation Effects. *Phys. Rev.* **1965**, *140*, A1133−A1138.

(77) Sun, J.; Ruzsinszky, A.; Perdew, J. P. Strongly Constrained and Appropriately Normed Semilocal Density Functional. *Phys. Rev. Lett.* **2015**, *115*, 036402.

(78) Kresse, G.; Furthmüller, J. Efficiency of Ab-Initio Total Energy Calculations for Metals and Semiconductors Using a Plane-Wave Basis Set. *Comput. Mater. Sci.* **1996**, *6*, 15−50.

(79) Kresse, G.; Joubert, D. From Ultrasoft Pseudopotentials to the Projector Augmented-Wave Method. *Phys. Rev. B* **1999**, *59*, 1758−1775.

(80) Sheppard, D.; Terrell, R.; Henkelman, G. Optimization Methods for Finding Minimum Energy Paths. *J. Chem. Phys.* **2008**, *128*, 134106.

(81) Clark, S. J.; Segall, M. D.; Pickard, C. J.; Hasnip, P. J.; Probert, M. I. J.; Refson, K.; Payne, M. C. First Principles Methods Using CASTEP. *Z. Kristallogr. Cryst. Mater.* **2005**, *220*, 567−570.

(82) Perdew, J. P.; Burke, K.; Ernzerhof, M. Generalized Gradient Approximation Made Simple. *Phys. Rev. Lett.* **1996**, *77*, 3865−3868.

(83) Pickard, C. J.; Mauri, F. All-Electron Magnetic Response with Pseudopotentials: NMR Chemical Shifts. *Phys. Rev. B* **2001**, *63*, 245101.

(84) Yates, J. R.; Pickard, C. J.; Mauri, F. Calculation of NMR Chemical Shifts for Extended Systems Using Ultrasoft Pseudopotentials. *Phys. Rev. B* **2007**, *76*, 024401.

(85) Yates, J. R.; Pickard, C. J.; Payne, M. C.; Mauri, F. Relativistic Nuclear Magnetic Resonance Chemical Shifts of Heavy Nuclei with Pseudopotentials and the Zeroth-Order Regular Approximation. *J. Chem. Phys.* **2003**, *118*, 5746−5753.

(86) Sadoc, A.; Body, M.; Legein, C.; Biswal, M.; Fayon, F.; Rocquefelte, X.; Boucher, F. NMR Parameters in Alkali, Alkaline Earth and Rare Earth Fluorides from First Principle Calculations. *Phys. Chem. Chem. Phys.* **2011**, *13*, 18539.